

TIME-DOMAIN SIMULATION OF VORTEX-INDUCED
VIBRATION FOR DEEPWATER MARINE RISERS

PETER MA



**Time-Domain Simulation of Vortex-Induced
Vibration for Deepwater Marine Risers**

by

©Peter Ma, B.Eng.

A thesis submitted to the
School of Graduate Studies
in partial fulfillment of the
requirements for the degree of
Master of Engineering

Faculty of Engineering and Applied Science
Memorial University of Newfoundland

February 2012

Abstract

The engineering challenges of Vortex-Induced Vibration (VIV) for marine risers are of great concern as offshore operations move into deepwater. The VIV phenomenon creates fatigue issues and could cause permanent damages in risers. An accurate tool for analyzing riser VIV is important for the safe operation of offshore drilling and exploration. Risers typically have an extremely large length-to-diameter ratio which makes direct scaling nearly impossible in physical model testing - this naturally requires the use of numerical methods.

In this work, a time-domain numerical model for simulating VIV of deepwater risers was developed. A novel forcing algorithm that utilizes the hydrodynamic coefficients of finite segments of a riser was adopted to predict the external forces on a riser due to fluid effects and riser motion. The predicted external forces are then applied on the riser. A global-coordinate-based finite element model was employed to compute the responses of the riser.

The computation consisted of a two step process: static and dynamic analysis. The static analysis iterates to find the equilibrium profile of the riser(s), then the dynamic analysis solves the equation of motion at each user-defined time step. The program outputs the responses and the reaction forces (tension) of the riser(s) at any user-defined nodes.

The numerical model was coded in Fortran 90 and validated by comparing program outputs with published experimental data. Validation studies were first conducted on mooring lines, and the comparison showed that the finite element method was able to

capture the nonlinear behaviour of these slender structures. With confidence in the finite element model, the VIV forcing algorithm was implemented in the program. Validation studies were then extended to the VIV prediction of a 6 meter rigid pipe with spring boundary conditions and a 13 meter laboratory scale top-tensioned riser. The comparisons between the predictions in this study with the experimental results are generally in good agreement.

Acknowledgements

I would like to express my sincere gratitude to my supervisor, Dr. Wei Qiu, under whose guidance and direction this research was carried out. Thanks to Mr. Don Spencer of Oceanic Consulting Corporation, for the theoretical lessons given at the beginning of this research.

This work was conducted at Memorial University of Newfoundland through fundings provided by Petroleum Research Atlantic Canada (PRAC), MITACS, and the Research and Development Corporation (RDC). I would like to gratefully acknowledge the fundings provided by PRAC, MITACS Accelerate Internship, the RDC Ocean Industries Student Research Award, and the fellowship from the School of Graduate Studies, Memorial University of Newfoundland.

I would also like to thank my colleagues in the Advanced Marine Hydrodynamics Laboratory, whom not only provided technical guidance on various numerical methods but also made the office a friendly place to work in. Also, special thanks to all other fellow graduate students for the help and support provided throughout the course of this study.

My deepest appreciation goes to my parents, sisters and Elim for their patience and support. They were always available when called upon, and made sure I stayed sane throughout the course of the program.

Contents

Abstract	i
Acknowledgements	iii
List of Figures	vii
List of Tables	x
Nomenclature	xi
1 Introduction	1
1.1 Background and Motivation	1
1.2 Marine Risers	3
1.3 Ocean Currents	5
1.4 Vortex-Induced Vibration	7
1.4.1 Stationary Cylinder VIV	7
1.4.2 Flexible Cylinder VIV	9
1.5 Riser Fatigue	10
1.6 Vortex-Induced Vibration Suppression	11
1.7 Deepwater Challenges	12
1.8 Outline of Thesis	14
2 Literature Review	16

2.1	Vortex-Induced Vibrations Prediction	16
2.2	VIV Prediction Methodologies	18
2.2.1	Computational Fluid Dynamics	19
2.2.2	Semi-empirical Models	23
2.2.3	Experimental Methods	25
3	Time-Domain Model	31
3.1	General	31
3.2	OCC's Forced Experiments	32
3.3	Time-Domain Forcing Algorithm	36
3.3.1	Surface Interpolation	39
3.3.2	Current Profile	42
3.4	Finite Element Methods	43
3.5	Summary of VIV Algorithm	44
4	MAPS-Mooring Validations	46
4.1	Catenary Mooring Line Excursion	46
4.2	Catenary Mooring Line Subjected to an Anchor Force	49
4.3	Forced Oscillation Experiment	50
4.4	Comparison with Full Scale Experiment	53
4.5	Comparison with Kitney and Brown's Experiment	58
5	MAPS-VIV Validation	63
5.1	Solid Cylinder VIV	63
5.2	Comparison with Chaplin's Experiments	68
5.2.1	General	68
5.2.2	Results for Case 1	72
5.2.3	Results for Case 3	75
5.2.4	Results for Case 6	77
5.2.5	Results for Case 9	79

5.2.6 Summary	81
6 Conclusions and Recommendations	84
References	87
A Mathematical Formulation	A-1
A.1 Coordinate System	A-1
A.2 Equations of Motion	A-2
B Numerical Methods	B-1
B.1 Finite Element Discretization	B-1
B.2 Formulation for Static Analysis	B-5
B.3 Formulation for Dynamic Analysis	B-8
B.4 Boundary Conditions	B-10
C Displacement Time Series Plots	C-1

List of Figures

1-1	Riser Types	3
1-2	Typical Deepwater Current Profiles (from Li, 2005)	6
1-3	Strouhal number versus Reynolds number for circular cylinders (from Blevins, 1990)	8
2-1	Numerical VIV Prediction Models	19
2-2	CFD Models	21
3-1	Oceanic Consulting Corporation's VIV test apparatus	32
3-2	Lift Force Coefficients	34
3-3	Venugopal Damping Model for Low and High Reduced Velocities	35
3-4	Lift Force Coefficients (Rotated View)	36
3-5	Zero Crossing Analysis of a Vibration Cycle (from Spencer et al., 2007)	37
3-6	Interpolation grid	41
3-7	Current profiles available in the present model	42
4-1	Top Tension Comparison of a Catenary Mooring Line	48
4-2	Top Tension Time Series for 0.15 forced motion amplitude at 0.48 Hz	52
4-3	Sensitivity to No. of Elements	55
4-4	Sensitivity to time step	56
4-5	Top Tension for Sample 2	57
4-6	Top Tension for Sample 3	57
4-7	Top Tension for non-dimensional motion amplitude of 0.03	59

4-8	Top Tension for non-dimensional motion amplitude of 0.05	60
4-9	Top Tension for non-dimensional motion amplitude of 0.07	60
4-10	Top Tension for non-dimensional motion amplitude of 0.09	61
4-11	Comparison of non-dimensional dynamic tension	62
5-1	Rigid riser VIV for uniform current speed of 1.1 m/s	65
5-2	Rigid riser VIV for uniform current speed of 1.6 m/s	65
5-3	Rigid riser VIV for uniform current speed of 1.8 m/s	66
5-4	Rigid riser VIV for uniform current speed of 2.4 m/s	66
5-5	Rigid riser VIV for uniform current speed of 2.6 m/s	67
5-6	Amplitude Ratio vs Nominal Reduced Velocity	68
5-7	Delft VIV experimental setup	70
5-8	Computational Model of the Delft Experiment	71
5-9	Case 1 Crossflow vibration envelope obtained from current model with 50, 100, 200 elements	73
5-10	Case 1 Time Series of Crossflow Vibration at the middle of the riser .	74
5-11	Case 1 Crossflow vibration envelope comparison between results from experiments, Shear7, Norsk Hydro, and the current model	74
5-12	Case 3 Crossflow vibration envelope obtained from current model with 50, 100, 200 elements	75
5-13	Case 3 Time Series of Crossflow Vibration at the middle of the riser .	76
5-14	Case 3 Crossflow vibration envelope comparison between results from experiments, Shear7, Norsk Hydro, and the current model	76
5-15	Case 6 Crossflow vibration envelope obtained from current model with 50, 100, 200 elements	77
5-16	Case 6 Time Series of Crossflow Vibration at the middle of the riser .	78
5-17	Case 6 Crossflow vibration envelope comparison between results from experiments, Shear7, Norsk Hydro, and the current model	78

5-18	Case 9 Crossflow vibration envelope obtained from current model with 50, 100, 200 elements	79
5-19	Case 9 Time Series of Crossflow Vibration at the middle of the riser .	80
5-20	Case 9 Crossflow vibration envelope comparison between results from experiments, Shear7, Norsk Hydro, and the current model	80
5-21	Max crossflow vibration across all models	81
5-22	Min crossflow vibration across all models	82
A-1	Coordinate System	A-2
B-1	Degrees of freedom for two rod elements	B-3
B-2	Flow Chart for Static Analysis	B-7
B-3	Flow Chart for Dynamic Analysis	B-11
C-1	Case 1 Time Series of Crossflow Vibration at 0.25L	C-2
C-2	Case1 Time Series of Crossflow Vibration at 0.75L	C-2
C-3	Case 3 Time Series of Crossflow Vibration at 0.25L	C-3
C-4	Case 3 Time Series of Crossflow Vibration at 0.75L	C-3
C-5	Case 6 Time Series of Crossflow Vibration at 0.25L	C-4
C-6	Case 6 Time Series of Crossflow Vibration at 0.75L	C-4
C-7	Case 9 Time Series of Crossflow Vibration at 0.25L	C-5
C-8	Case 9 Time Series of Crossflow Vibration at 0.75L	C-5

List of Tables

4.1	Parameters of a Catenary Mooring Line	47
4.2	Results for Catenary Line subjected to horizontal anchor force	50
4.3	Parameters used in Faure's Forced Oscillation Experiment	51
4.4	Parameters of the mooring system onboard SSV Henrik Ibsen	53
4.5	Environmental loads for Full Scale Experiment	54
4.6	Measured vs. MAPS-Mooring Tension	58
4.7	Full Scale Characteristics of Kitney and Brown's Experiment	59
5.1	Solid Cylinder Properties	63
5.2	Properties of the riser used in the Delft VIV experiment	69
5.3	Current speed and top tension of the Delft VIV experiments	70

Nomenclature

CFD	Computational fluid dynamic
CVAR	Compliant vertical access riser
DNS	Direct numerical simulation
EoM	Equations of motion
FD	Fatigue damage
FEM	Finite element model
FL	Fatigue life
HCR	Highly compliant riser
JIP	Joint industry project
LES	Large eddy simulation
MODU	Mobile offshore drilling unit
RANS	Reynolds averaged Navier Stokes
Re	Reynolds Number
SCR	Steel catenary riser
St	Strouhal number
TLP	Tensioned-leg platform
TTR	Top-tensioned riser
VIM	Vortex-induced motion
VIV	Vortex-induced vibration

A	amplitude of vibration
A^*	cross flow amplitude ratio
A_k	interpolation function
B	buoyancy force per unit length
C_D	Drag coefficient
C_{D0}	Steady drag component
C_{LV}	Lift coefficient
C_M	Added mass coefficient
D	Diameter of the riser
$D(t)$	Time-dependent drag force
E	elastic modulus of the riser
f_0	frequency of oscillation
f_n	Natural frequency
F	resultant force
F^d	hydrodynamic force per unit length
F^s	hydrostatic force per unit length
H	torque
I	moment of inertia of the cross section
L	length of the element
$L(t)$	Time-dependent lift force
M	resultant moment
N_k	shape functions of a quadrilateral
P_m	interpolation function
P_s	hydrostatic pressure
R	radius of the riser
T	tension
\bar{T}	effective tension
T_0	Period of oscillation
U	Flow speed

U^*	Reduced velocity from free vibration
U_{ik}	coefficients in interpolation functions
\mathbf{V}	total water particle velocity
V_t	tangential velocity
V_{rel}^n	relative fluid velocity normal to riser
$\dot{\mathbf{V}}$	total water particle acceleration
$\dot{\mathbf{V}}^n$	water particle acceleration normal to riser
V_R	Reduced velocity from forced vibration
\mathbf{m}	applied moment per unit length
q	applied force per unit length
\mathbf{r}	position vector of riser
r_i	component of \mathbf{r} in i^{th} direction
$\dot{\mathbf{r}}$	velocity of riser
$\dot{\mathbf{r}}^n$	normal velocity of riser
$\ddot{\mathbf{r}}$	acceleration of riser
$\ddot{\mathbf{r}}^n$	normal acceleration of riser
\mathbf{r}'	unit tangent vector
\mathbf{r}''	principal normal vector
s	arclength along the riser
t	time
\mathbf{w}	weight per unit length
$\tilde{\mathbf{w}}$	effective weight
κ	curvature
λ	Lagrangian multiplier
λ_m	coefficient in interpolation function
μ	Kinematic viscosity of water
ρ	mass per unit length
δ_{ij}	Kronecker Delta function

Chapter 1

Introduction

The analyses of the behaviour of risers operating in high current environment is a critical part of the riser design process. Engineers must analyze the potential risks that these riser systems might be subjected to, and design to mitigate such risks for operation. One of the main design issues for marine risers, such as steel catenary risers, is the accurate evaluation of fatigue life due to vortex-induced vibrations. This depends on the accuracy of VIV response prediction models.

Various prediction tools for analyzing vortex-induced vibrations have emerged from decades of research and development, but offshore operations still identify gaps between the predicted responses and those observed in the field. Vortex-induced vibrations on risers is well-known, but it is a difficult problem for analysis and prediction. The physics behind this phenomenon is not fully understood; hence the prediction models for VIV are inadequate for new designs and risers operating in deepwater.

1.1 Background and Motivation

Marine risers operating in the vertical water column are exposed to current flow. The combination of current speed, riser geometry and surface roughness causes vortices to

be shed in the vicinity of the riser. When the vortex shedding frequency approaches one or more of the natural frequencies of the riser, resonance vibration takes place. This phenomenon is known as **lock-in**. When lock-in occurs, the vortex shedding frequency is controlled by the vibration frequency. This creates a force feedback phenomenon on vortex motion and structure motion. Under certain conditions, risers vibrate at large amplitudes once they reach the lock-in zone. When multiple risers are located in close proximity in deepwater, VIV can potentially lead to the clashing of adjacent risers. This would lead to suspension of offshore operation, or result in serious financial loss and environmental damage if the riser(s) break off due to fatigue issues.

The VIV on risers are further complicated by uncertainties in current flow. Current velocities are both spatially and temporally variable, and their magnitude and directions may be random, making VIV predictions even more difficult. Most of the research on VIV assumes a constant or sheared current profile, to reduce technical challenges in experimental and numerical prediction. This, however, is never the case encountered in offshore.

VIV analysis has been conducted using both physical testing and numerical models. Physical testing, though believed to be more accurate, is generally not cost effective and requires special testing facilities. Computational fluid dynamic (CFD) models are not practical due to limiting computer resources and at present can only capture VIV at relatively low Reynolds (Re) number flows. High Re number flows in CFD are the goal of future development (Lie et al., 2011).

The common industry practice for analyzing riser VIV is the use of semi-empirical linear modal frequency models. These models, developed decades ago, were tailored to predict VIV on vertical top-tensioned risers subjected to uniform or sheared current flows. As operations move into deeper water, vertical top-tensioned risers might no longer be feasible due to complex environmental constraints and the type of floaters these risers are connected to. Therefore, the modal frequency approach is insufficient

to simulate VIV for deepwater risers. To eliminate the limitations of linear approaches and overcome some of the challenges mentioned, an efficient time-domain model is developed in this work. This approach takes into consideration the nonlinearities from riser geometry, sea bottom conditions, and environmental loads. The developed model can be easily incorporated into design of risers with strakes and fairings.

1.2 Marine Risers

Risers are used to transport fluids (hydrocarbon, drilling fluids, etc.) from subsea facilities to a surface vessel or vice versa during offshore operations. Riser concept selections are mainly based on the type of floater (vessel) employed, their respective motion characteristics, and the water depth of the field.

As shown in Figure 1-1, there are four main types of risers commonly employed in offshore operations. Mobile offshore drilling unit (MODU) risers are the risers used at the early age of offshore exploration. This is a type of top-tensioned riser (TTR) but its design has been refined since the early 1960s (Boster et al., 2004).

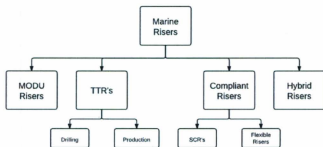


Figure 1-1: Riser Types

The second type is TTR. They can be drilling or production risers or a combination of both. TTRs are most commonly used on spars or tension-leg-platforms (TLP) due to these vessels' low heave characteristics. These risers require the surface vessel to possess good motion characteristics. While being entirely vertical, these risers are also susceptible to lateral movement when subjected to wind and wave loads. As a result, they can experience significant loads at the top and also at the touch-down point. A common practice to reduce these high loads is to fit buoyancy cans at certain points on the risers to increase the buoyancy force and offset the weight. In addition, motion compensators can also be employed to keep constant tension loads in the risers by moving the facilities vertically as needed.

The compliant risers consist of steel catenary risers (SCR) and flexible risers. In deeper waters, SCRs are commonly used on TLPs, FPSOs, spars, and fixed structures. Due to the curved nature of these risers, these risers can handle some lateral movement but are vulnerable to large movements. Flexible risers are used in shallower water or in operations where the flexible characteristics are required. Their ability to tolerate lateral and vertical movements make them suitable for floating vessels that are prone to more motion. There are different configurations for flexible risers, such as steep S, lazy S (both use anchored buoyancy modules), steep wave and lazy wave (both with buoyancy modules). These configurations help to reduce the impacts on flexible risers when they are exposed to external loads. Hybrid risers have been employed for deepwater operations. The arrays of steel pipes, connected to the seabed, are vertically supported by external buoyancy modules and connected to the surface vessel by flexible jumpers. The buoyancy modules are installed at a depth well below the free surface, preventing the steel risers from experiencing wave loads. This type of configuration minimizes the impact from vessel motion-induced vibrations in risers. Another advantage of this type of risers is the reduction in bending stresses at the top and touch-down points. These systems require, however, a more complicated installation process and higher installation cost.

1.3 Ocean Currents

Ocean currents play an integral role in offshore systems design; they are one of the main sources of environmental loads. The design of any offshore structure or subsea system must take current into account, throughout the entire design process, to ensure the integrity of such systems is not influenced by extreme current conditions. In some cases, due to operational demands, some systems must also withstand high current without jeopardizing operations.

Ocean currents are the movement of water when acted upon by external forces. These external forces include Coriolis, pressure gradient, friction, and centrifugal forces. The Coriolis forces are due to the rotation of the earth around its axis. As a result, the ocean waters move to the right in the northern hemisphere, and to the left in the southern hemisphere. The amount of movement depends on flow speed and the location along the latitudes (Randall, 1997).

The pressure gradient forces arise due to the horizontal change in pressure between high and low pressure flows. The difference in pressure causes the water to flow from high pressure areas to lower pressure parts. The magnitude of flow depends on the magnitude of the pressure gradient in all three directions.

Friction forces are the consequences of turbulent eddies interacting with the mean flow and initiating frictional effects in the flow. Earth's rotation along its tilted axis generates a centrifugal force that also influences current flow. The centrifugal force generated has a strong vertical component (gravity) while the horizontal component is negligible.

The existence of these forces cause ocean current to exhibit irregular patterns along the water column. A typical chart to describe current of a region in the ocean is a current profile. An ocean current profile provides engineers with average current velocities along the water column. This information is used to evaluate the behaviour of risers subjected to these loading conditions.

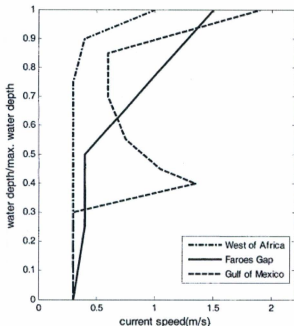


Figure 1-2: Typical Deepwater Current Profiles (from Li, 2005)

Due to the fact that risers have large aspect ratio (length/diameter), they tend to be vulnerable to current loads. Ocean currents are the main driver for inducing vibrations in risers. In addition, current profiles vary from region to region. Figure 1-2 shows typical current profiles for the Gulf of Mexico, West Africa and Faroes Gap. The sharp changes in current speed along the water column, in the Gulf of Mexico for instance, can induce local vibrations at some lengths along the riser. Once local VIV develops, and under certain conditions, it tends to propagate through the entire riser and produce vibration of the entire riser. In addition, a critical current profile to consider in the design process for the Gulf of Mexico is the loop current, as shown

in Figure 1-2. This is a spatially varying current, having eddies attached to it, and has high surface velocities. The combination of loop current and big waves can pose potential risks to offshore structures and this is usually the limiting environmental load case in riser designs. The numerical model developed in this work will take arbitrary current profiles into consideration, therefore it is not limited to uniform or sheared current profiles.

1.4 Vortex-Induced Vibration

VIV occurs in many fields of engineering from power cables to heat exchanger arrays to marine risers. Unlike many vibration problems in which the exciting force is independent of the structure motion itself, the exciting force in VIV is a function of motion parameters. In other words, VIV is self-excited since the motion itself gives rise to the exciting force.

1.4.1 Stationary Cylinder VIV

For a free stream with speed, U , moving past a stationary cylinder with diameter D , pressure in the fluid particles changes and approaches the stagnation pressure at the leading edge of the cylinder. This increase in pressure slows the incoming flow forward and forms boundary layers on both sides of the cylinder. In high Reynolds number flows, the boundary layers separate near the widest area (side) of the cylinder which results in the formation of two shear layers aft of the flow. The inner shear layer moves at a much smaller rate than the outer layer; hence, these layers then slip into the wake region and forms vortices (Blevins, 1990).

For a stationary cylinder subjected to a uniform flow, vortices are shed at a frequency that is proportional to the ratio of current speed to cylinder diameter.

$$f_s = St \frac{U}{D} \quad (1.1)$$

where St is the Strouhal number which depends on the Reynolds number of the flow and the surface roughness of the cylinder, as shown in Figure 1-3. In the figure, the lower boundary shows the St plot for a rough cylinder and the upper boundary is the St dependence on Re for a smooth cylinder.

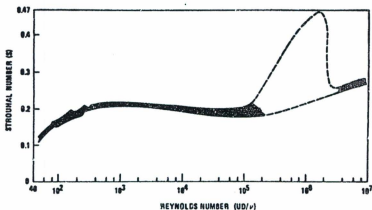


Figure 1-3: Strouhal number versus Reynolds number for circular cylinders (from Blevins, 1990)

The Reynolds number of a flow is a dimensionless quantity that is defined as the ratio of inertial forces to viscous forces, as shown in Equation 1.2.

$$Re = \frac{UD}{\mu} \quad (1.2)$$

where μ is the kinematic viscosity.

For steady current flows, there are generally four flow regimes identified by their corresponding Re range. In the sub-critical range, $300 < Re < 150,000$, boundary layer is laminar until separation occurs at approximately 80° aft of the cylinder stagnation point. Vortex shedding in this range is periodic and strong (Blevins, 1990). The drag coefficient in the sub-critical range is almost constant at a value of 1.2.

The Re range between 150,000 and 3,500,000 is called the transitional regime. The boundary layer around the cylinder is unstable, separates, and then becomes turbulent. Separation occurs at 140° aft of the stagnation point. The drag coefficient drops to about 0.3. The three-dimensional effect of vortex shedding arises, and eventually upsets the regular shedding process and gives a wider array of shedding frequencies.

All flows above an Re of 3,500,000 are called supercritical in VIV studies. In this range, the vortex shedding is re-established with a turbulent boundary layer. The vortex shedding frequency is highly variable and the wake behind the cylinder is no longer organized.

1.4.2 Flexible Cylinder VIV

Flexible or flexibly mounted cylinders add another level of complexity. Flexibility means the vortex shedding will produce more cylinder motion, which will in turn disrupt the vortex shedding pattern described in the previous section. The vortices shed behind flexible cylinders interact with, and excite, the cylinder in both the drag (inline) and lift (cross flow) directions - and the motion of the cylinder in turn disrupts the vortices - forming a coupled force feedback phenomenon known as vortex-induced vibration.

When vortices are shed at frequencies close to the natural frequencies of the cylinder, lock-in occurs. The vortex shedding frequency is then synchronized with the structural vibration frequency, producing large-amplitude vibrations. However, this increase in amplitude of vibration is limited by the increase in hydrodynamic damping associated with the larger structural oscillation as well as the self-limiting nature of vortex strength. This self-limiting nature of VIV usually limits the vibration amplitudes to be less than 1.1 times the diameter. In addition, lock-in is also associated with an increase in the correlation length, vortex strength, as well as the amplification of drag loads.

Experiments have shown that lift forces on cylinders subjected to VIV occur at the vortex shedding frequency. The drag forces; however, were witnessed to oscillate at twice the vortex shedding frequency. This implies that vortices, traveling in the inline direction, are shed from the cylinder with half the vortex shedding period ($T/2$). This is because of the alternate shedding of vortices in the inline direction. Due to the asymmetric nature of vortex shedding in the crossflow direction, the lift force is shed at a period of T . Hence the direction of the lift force depends on which side of the cylinder from which the vortices are shed (Faltisen, 1990). This will be reflected in the hydrodynamic forces formulation in the later sections.

1.5 Riser Fatigue

The design of risers is an iterative process. With the help of API or DNV standards (API RP 2RD or DNV OS F201), initial sizing of riser(s) is obtained based on specifications and the environment in which the riser(s) will operate. Once the sizing is known, analyses are extended to static analysis (configuration), storm analysis, VIV analysis, vessel motion induced fatigue, and VIM analysis. The fatigue damage induced from VIV, VIM, and first and second order waves must satisfy design standard recommendations before the design iteration is completed. Typically, these standards require a design life of greater than 200 years for a 20 year service. The fatigue life at any given point is given by

$$FL = \frac{1}{FD(VIV + VIM + WaveInduced)} \quad (1.3)$$

where FL is the total fatigue life, and FD is the fatigue damage from VIV, VIM, or wave induced loads. Fatigue damage is a result of stress fluctuations that cause small defects in the riser material to grow. This can lead to riser failure over time. The fatigue life of riser systems are often dominated by VIV.

To make accurate fatigue life predictions, the VIV responses must be accurately

assessed to avoid over or under designs. If the VIV response under predicts, the fatigue life will increase and result in possible failure during its service life. For conservative predictions, the fatigue life will decrease and result in an over design. The prediction of VIV plays a major role in determining the fatigue life of risers during the design process, and helps engineers to arrive at cost effective and safe designs.

1.6 Vortex-Induced Vibration Suppression

Riser designs usually fail to meet fatigue criteria set by API or DNV standards after completing the first fatigue analysis. Designers may choose a number of ways to improve the fatigue life of the riser being designed. Theoretically, VIV can be suppressed by increasing the amount of damping (structural and hydrodynamic), increasing the stiffness, and decreasing flow separation (Blevins, 1990).

The designer may choose to modifying the mass and tension of the riser. The former can be done by changing the size of the riser or by subtracting buoyancy. The latter can be achieved by modifying the stiffness through pre-tensioning of the riser. Based on a Strouhal number (≈ 0.2), the pre-tensioning will change the natural frequencies of the riser away from the Strouhal frequency. This will avoid vortex induced resonant oscillations in both the inline and cross-flow directions when subjected to current loading.

In addition to adjusting the natural frequencies of the riser, a more common approach is through the use of vortex suppression (add-on) devices such as strakes, fairings, or combination of the two. These devices are fitted around the riser. Their existence prevents the formation of an organized vortex street and reduces vortices formed in the vicinity of the riser.

Strakes

Strakes act to disrupt the flow pattern around the riser and produce weaker vortices. This can successfully reduce the vortex shedding forces. However, one drawback of

strakes is that they tend to increase the drag load on the riser. This increase in drag load can potentially lead to clashing of adjacent risers (Bai and Bai, 2005). This increase in drag load is still lower than that experienced by a bare pipe undergoing VIV.

Fairings

Fairings are fitted around risers and act to streamline the flow around risers and consequently reduces vortex shedding. These devices are free to rotate around the riser; therefore, they adjust directions depending on the direction of the incoming current. They are most effective at suppressing vortex shedding when the risers are vertical or almost vertical. As a result, they are more commonly seen on TTRs and vertical parts of SCRs.

There are also disadvantages of using fairings. The most important one is the induction of a complex phenomenon known as galloping. This is generally caused by instability of the structure when subjected to current flow. Galloping vibration is different from VIV in that it does not require the vibration frequency to reach the natural frequency of the structures. It is also self-excited, and generally possesses an oval vibration shape. Fairings are also less reliable due to its freedom to move around the riser's central axis; therefore, VIV may or may not be suppressed.

Forced vibration experiments have also been performed on strakes and fairings, and the corresponding hydrodynamic force coefficients have been collected as a function of reduced velocities and amplitude ratios. These coefficients can also be used as input in the program being developed in this work, and predict responses for risers with strakes or fairings.

1.7 Deepwater Challenges

In shallower water applications, vibrations on risers with shorter lengths can be captured using a linear modal frequency approach - such as the program Shear7.

In deepwater operations, much longer risers are adopted for various applications. The prediction of riser VIV for deepwater risers is more complicated. Due to load and geometric nonlinearities, the linear frequency approach is no longer valid.

Deepwater risers are subjected to flow (current and wave) variation along their length, as well as possible vessel-induced motion from the top. We can consider two response regimes: lock-in is not initiated, and lock-in takes place along a particular span of the riser.

According to the work of Vandiver (1993), lock-in may not occur given one or more of three conditions: (1), the damping is sufficiently large to suppress flow-induced motion, (2), the vortices do not shed at the natural frequency of the mode(s), and/or (3), wide excitation bandwidth covering the natural frequencies of multiple modes - giving rise to random vibrations along the length of the riser. The first two reasons are easily understood and implemented in numerical models. The third reason is highly nonlinear and difficult to predict, and it depends on the flow characteristics and the number of resonant natural modes, this requires a detailed account for the material properties of the riser as well as accurate representation of current flow.

Lock-in, however, is more likely to occur in deepwater for several reasons. Current speeds are higher in deepwater than many shallow water locations (Allen, 1998). The increase in slenderness ratio (L/D) reduces the natural frequencies of risers thus allowing even lower current speeds to induce VIV. The variation in current along the longer water depth, is likely to excite multi-modal responses along the riser. Additional complexity arises when multiple risers, operating along the water column, interact with each other (interference). For instance, wake induced vibrations on a riser, in tandem with another riser, can increase the magnitude of riser vibrations. Wake induced vibrations can also amplify drag forces and cause riser clashing.

The highest level of uncertainty and high stress occurs at the touchdown point or the fairlead connection point of SCR in deepwater. The SCR responses in these regions are characterized by intermittently laying and lifting motions (Grant et al.,

2000). This is another reason that frequency domain solution is not adequate, as it requires the touchdown point to be fixed.

For deepwater riser VIV analysis, it is desired to have a numerical model that is not restricted in load and geometric nonlinearity, is able to model dynamic boundary conditions (i.e. changing touchdown points), and the VIV forcing algorithm should cover a range of lock-in and non-lock-in behaviours.

1.8 Outline of Thesis

The scope of this work includes the development of a time-domain code for the analysis of riser vortex-induced vibrations. With the aid of advanced numerical methods and high quality test data, an efficient and accurate semi-empirical time-domain program is developed. This program eliminates many of the limitations of the traditional linear modal frequency approach. This thesis is subdivided into 6 chapters to logically present the rationale behind the research, mathematical formulation, and the results obtained from this research.

Chapter 2 gives a literature survey of the methodologies adopted in riser VIV research and the current industry practice. This will include discussion on three classes (CFD, semi-empirical, and experimental) of prediction models.

Based on the literature reviews and a collection of experimental data, Chapter 3 presents the new approach adopted in this research. The rationale behind the selected approach, the acquisition of experimental data, as well as the numerical method adopted will be discussed in detail.

The VIV code is implemented using Fortran 90. Validation studies are given in Chapter 4 and Chapter 5. Chapter 4 presents the validation of the program for mooring lines (excluding the VIV part), and Chapter 5 presents validation study for riser VIV.

The robustness of the program was first shown by its application to various static

and dynamic problems, and its extension to analyze VIV of risers. Conclusions and recommendations for further development are drawn in Chapter 6.

Appendix A presents the derivation of the equations of motion of a rod. Finite Element discretization of the equations of motion and program flow charts are shown in Appendix B.

Chapter 2

Literature Review

Research and development work on VIV began nearly a century ago. There is a large body of published literature available on the topic. The literature review in this work, therefore, must be selective. Instead of focusing on the physics of VIV, this review is conducted on VIV prediction methodologies and approaches that are applicable to the field of offshore and ocean engineering. The review examines both numerical and experimental VIV prediction approaches adopted by researchers, and their respective strengths and weaknesses. The review is also extended to VIV suppression methodologies.

2.1 Vortex-Induced Vibrations Prediction

The accurate assessment of VIV fatigue requires accurate computation of riser VIV responses. There are a number of factors that influence the accuracy of VIV prediction models. As noted in the work of Allen (1998), the accurate account of the parameters listed below have a direct impact on the accuracy of riser VIV prediction:

1. current profile
2. excitation and correlation length of lift forces and vortex shedding

3. frequency and magnitude of the lift force exerted on the riser as a result of vortex shedding
4. hydrodynamic damping
5. riser structural properties and geometry

Current profile is the most influential factor in VIV prediction. For constant diameter and surface roughness, current speed will determine whether riser VIV will take place or not. For long flexible risers with low natural frequency modes, low current can theoretically excite VIV.

In semi-empirical models, excitation lift forces are obtained through forced vibration experiments. These forces are functions of non-dimensionalized amplitude ratio and reduced velocity. Traditionally, the excitation length of these lift forces in the spanwise direction must also be accounted for in these models. Correlation arises from the three-dimensional nature of wake structures behind cylinders. A correlation of 1.0 implies two-dimensional flow. Under given flow conditions, correlation in the spanwise direction is usually described by empirical correlation functions that depend on amplitude of vibration and spanwise spacing. The correlation length is then defined as the area under both sides of the correlation function (Blevins, 1990). The correlation length of vortex shedding is not necessarily the same as the excitation length that is subjected to lift forces. Therefore, accurate estimation of VIV responses require an appropriate account for correlation lengths.

Hydrodynamic damping, depending on current profiles, is usually much higher than structural damping. Like lift and drag forces, hydrodynamic damping also depends on the amplitude ratio and reduced velocity. In other words, the amount of damping depends on the amplitude and frequency of vibration of the riser. The computation of damping is further complicated by the location (spanwise) along the riser at which damping applies. One of the significant weaknesses of most commercial VIV softwares lies in their implementation of the damping model.

Riser geometry and material properties must also be correctly modelled. The mass, stiffness and bending characteristics must be correctly accounted for. These properties will determine the natural frequencies and the corresponding mode shapes of the riser. The natural frequencies are inversely proportional to length and mass and proportional to tension and bending stiffness. This is generally captured using the finite element method.

2.2 VIV Prediction Methodologies

The two main approaches to study the riser VIV phenomenon are the use of numerical models and physical experiments. Physical testing is utilized to study VIV to understand the global responses of a riser design and in some cases support numerical modeling. In addition, physical data are useful for validating numerical programs. However, these experimental data sets are very limited due to proprietary reasons, technical challenges in lab testing, and expenses associated with large-scale field testing. Consequently, research has been focused on developing numerical models for VIV analysis in a cost-effective and efficient manner.

Numerical models are useful for understanding VIV in the absence of physical testing. Most of the research conducted on VIV has been focused on the numerical modeling of this complex phenomenon. The available numerical models are summarized in Figure 2-1.

CFD has been gaining popularity as a tool for VIV research due to advances in computation power. As shown in the figure, CFD research has been focused on 2D and 3D simulations. On the other side of the chart are the semi-empirical models. These models include both linear frequency simulation as well as time-domain simulations. These models are discussed in the following sections.

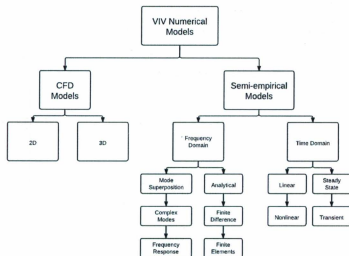


Figure 2-1: Numerical VIV Prediction Models

2.2.1 Computational Fluid Dynamics

Simulating phenomenon such as vortex shedding around cylinders requires the capturing of the behavior of turbulent eddies as the flow interacts with the structure. In CFD simulations, this is conducted using advanced computational techniques to model turbulent flow. There are a number of these models available and each have their limitations and strengths. Figure 2-2 shows a flow chart of these CFD models available in the literature. There are three main types of CFD models used in VIV research, namely Reynolds Averaged Navier Stokes (RANS), Large Eddy Simulation (LES), and Direct Numerical Simulation (DNS). Since CFD is not the core of the current research, these models and their applications to VIV are only briefly described.

RANS computes the 'averages' of all the unsteadiness in a turbulent flow. In RANS formulation, the variable of interest may be written as the sum of a time-varying part plus a fluctuating component (Ferziger and Perić, 2002). In essence, it computes the averaged Reynolds stress of a turbulent flow. Under RANS, there are three main subcategories of models: Linear Eddy Viscosity, Nonlinear Eddy Viscosity, and Reynolds Stress.

To obtain more details than the level that RANS computes, a LES model may be employed. LES is based on the notion that the motions of large eddies play a much larger role in carrying the conserved properties of the entire flow and that smaller eddies are less energetic and contribute less to the properties of the flow. In an LES model, filtering is used to separate the large and small eddies in a turbulent flow. This allows LES to explicitly solve for the large eddies and compute the smaller eddies implicitly using a subgrid-scale model. Some of the subgrid-scale models are shown in Figure 2-2 under LES. These subgrid-scale models are empirical. Therefore, LES simulates the large eddies more precisely than the smaller ones (Ferziger and Perić, 2002). This approach is 3-dimensional, time dependent and computationally intensive. However, LES is very attractive when simulating high Reynolds number flows with complex geometry.

The highest level of detail a turbulence model can provide is through the use of a DNS model. DNS does not approximate nor average the motions of eddies, be it large or small scales. All the details of the turbulence are captured; therefore, the computational domain must be as large as the physical domain. This requirement puts a constraint on the simulation as the number of grids (computational domain) is directly dependent on computer capacity.

Most of these models are still at the research stage and have not been adopted for design due to several reasons. These models are computationally intensive, it takes a long time to arrive at a solution and the results are very sensitive to user inputs. Some of the models, such as LES and DNS are still only applicable for relatively

low Reynolds number flows. Critical Reynolds number flow has not been available in DNS models due to lack of computer capacity. Research continues in CFD for VIV computation with the hope that computer hardware will be able to handle DNS simulations at high Reynolds number flow in the near future. CFD studies on cylinder VIV for various configurations (stationary cylinder, oscillating cylinder, and multiple cylinder simulations) are summarized in the following sections.

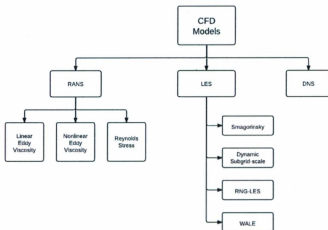


Figure 2-2: CFD Models

Simulation of a flow past a stationary cylinder using LES or DNS gives researchers some interesting insights on the behaviour of eddies in the vicinity of the cylinder and how they interact with the cylinder itself. While it is not feasible to use DNS for critical and high Reynolds number flows, most of the research to date has been focused on simulation using LES.

Athuri et al. (2009) utilized a 2D LES Smagorinsky model to study the wake

structure of a cylinder forced to oscillate and the same cylinder that was self-excited. The Reynolds number range of 500-8000 was conducted, and the influence of Re on the wake structure was investigated. The influence of oscillation frequency and Reynolds number on the wake behaviour was shown with 2D simulations, but a precise comparison with experimental results is not possible as the 3D effects on the wake structure was not accounted for.

He et al. (2010) simulated VIV of a flexible riser, with an aspect ratio of 250, in uniform current flow at a Reynolds number range of 100 - 12500. In their work, the riser structure was modeled using a finite element method (FEM) and the finite volume method was adopted to discretize the fluid domain. The model is based on the assumption that the flow is locally 2D and strip theory is adopted along the spanwise direction of the riser. At a Strouhal number of about 0.17, they found that the envelope of vibration in the cross-flow direction is approximately 4-6 times the envelope of inline vibration. The maximum cross-flow amplitude was about 1.2D and 0.25D for the inline direction.

Multiple cylinder simulations are also performed with 2 or more cylinders arranged in a desired configuration. The main configurations are cylinders arranged in tandem, side-by-side, and staggered. Carmo et al. (2011) carried out 2D and 3D DNS of two cylinders in tandem. In their simulation, the upstream cylinder is fixed while the cylinder in the downstream wake is free to oscillate in the transverse direction. The 2D simulation was done at a fixed Re of 150 and the 3D simulation was conducted at an Re of 300 while the reduced velocities were varied by changing the structural stiffness. The responses of the downstream cylinder were compared with the responses of a single elastically mounted cylinder. It was shown that the cylinder in the tandem configuration experienced higher amplitudes of vibration and a wider lock-in envelope. The authors believed this difference was due to the oscillatory flow in the gap of the tandem configuration. This gap forced the stagnation point to alternate along the front wall of the downstream cylinder.

Recent CFD research on VIV has shown that the current state-of-the-art is limited by computer capacity. The highest Reynolds number flow computed for VIV studies is limited to around 15000 for LES models and less than 1000 for DNS models. This is far below the Re range observed in the offshore, which is usually beyond one million. Consequently, CFD approaches have not been adopted for riser VIV analysis in design (Lie et al., 2011).

2.2.2 Semi-empirical Models

Research on VIV in the last few decades has led to the commercialization of a number of VIV prediction programs that have been adopted by the offshore industry. The common theme behind these software packages is that they all make use of experimental hydrodynamic coefficients along with numerical techniques to evaluate VIV responses. Hence they are “semi-empirical” models. Due to differences in the assumptions, analytical framework, and empirical information used in these models, there has been large scatter in predictions from these models (Larsen and Halse, 1997).

The most commonly used VIV program in the industry is SHEAR 7. This program, developed at the Massachusetts Institute of Technology (MIT), solves the cross flow vibration of a cylinder experiencing VIV. The numerical model in SHEAR 7 uses a mode superposition method and pre-determines the number of modes that are likely to be subjected to VIV and computes the cross-flow vibration based on empirical hydrodynamic coefficients. Based on user input data, SHEAR 7 computes the potentially excited modes. A mode cutoff treatment is utilized based on input power for the identified modes. If more than one mode is excited, the overlaps between the modes are eliminated. The program then computes the modal input power (excitation), and the modal output power (damping). Modal power balance is then done by iteration until the VIV amplitude ratio (A/D) converges. At each iteration, the program adjusts the lift coefficient and iterates till convergence (Vandiver and

Li, 2005). SHEAR3D is another model developed at MIT (Venugopal, 1996) as an extension of SHEAR 7. As noted above, SHEAR 7 is only a cross-flow prediction program. Realizing the inadequacy of the 2D model, Venugopal extended the model to a 3D model by including the responses in the inline direction. A different damping model was also presented in his work.

A second semi-empirical model is VIVA or VIVARRAY, which was also developed at MIT. VIVA evaluates the riser response using complex harmonic modes. The amplitude and phase of each mode vary along the length of the riser, so they can either be standing waves, travelling waves, or a combination of the two.

VIVANA, developed by MARINTEK, is an FEM based program for analyzing riser VIV. This program is not a stand-alone program in the sense that the analysis must be done with the aid of RIFLEX. RIFLEX is an FEM package developed for the static and dynamic analysis of slender marine structures. VIVANA also utilizes a modal or eigenvalue approach for VIV analysis. Static analysis and eigenvalue analysis are first conducted using RIFLEX. VIVANA then identifies the possible excitation frequencies as well as the dominating ones and computes the VIV responses for each identified frequency. Based on these responses, fatigue analysis is carried out. This program is also based on a linear frequency domain approach, and neglects the nonlinearities of the problem.

Another class of models is the Wake Oscillator Model. This was first proposed by Bishop and Hassan (1964) and later adopted by Iwan and Blevins (1974). The Iwan-Blevins model, as utilized in the commercial software OrcaFlex, utilized forced experimental data conducted in the Reynolds number range of 10^3 to 10^5 . In their work, the governing equation of a self-excited fluid oscillator was derived. This governing equation, along with the equation of cylinder motion formed the basis of the numerical model.

Recently, researchers have extended these semi-empirical models to time-domain simulations. Grant et al. (2000) developed a time-domain VIV solver, ABAVIV.

This program uses the finite element package ABAQUS along with a VIV algorithm to simulate riser VIV responses in the time-domain. The VIV algorithm used in ABAVIV is based on a correlation model proposed by Blevins (1990). The cross-flow vibration is excited and monitored to determine if it is within a pre-defined lock-in criterion. When lock-in criterion is met, the algorithm smoothly tunes the lift force to be in phase with the riser vibration velocity. If not, the algorithm uses the Strouhal frequency as the lift force frequency and assigns it a random phase angle for each correlation length along the riser (Grant et al., 2000). The determination of the lock-in region, therefore, requires the VIV frequency, amplitude and phase. ABAVIV uses exponential modeling techniques to determine these parameters, based on the time-history of vibrations. This model was shown to capture VIV reasonably well for a few riser configurations. The program, however, is based on the assumption that vortices are shed at a frequency corresponding to a Strouhal number of 0.17. This may not be valid when the riser motion significantly influences the vortex shedding pattern. ABAVIV also assumed the added mass to be independent of reduced velocities, and assigns a value of 1.0.

A recent contribution to time-domain VIV prediction is a program called SimVIV (Sidarta et al., 2010). Similar to ABAVIV, SimVIV adopts ABAQUS as the finite element engine and uses a user-subroutine to compute the VIV forcing. SimVIV was shown to compute both inline and cross flow VIV. The cross flow vibration is based on the same theory used in ABAVIV. The inline response was simulated, but more calibration data is required to improve the accuracy of the predicted responses in the inline direction.

2.2.3 Experimental Methods

Experimental methods provide physical means of collecting meaningful insight on the behaviour of risers subjected to VIV. There are four main types of experiments in VIV studies. The forced vibration experiments are conducted to acquire hydrodynamic

coefficients on the cylinder subjected to forced vibration. These coefficients are used in semi-empirical numerical models to predict riser VIV response. The second type of experiment is the free vibration experiments. In the free vibration experiments, the cylinder is not forced to vibrate and therefore captures the "real" VIV responses of the cylinder. Both forced and free vibration experiments use rigid pipes to gain overall behaviour of a segment of a long riser. Laboratory scale riser testing are conducted on a shorter riser that are scaled to accommodate the testing facilities. Full scale riser testing are normally done in the ocean due to limiting size of controlled laboratory facilities. Both of these types of testing are challenging, but extremely useful for benchmark validation of numerical models.

Forced Vibration Experiments

Forced vibration experiments are conducted on finite lengths of a cylinder in which the cylinder is forced to oscillate at a prescribed amplitude and frequency while being towed through water (Sarpkaya, 1978; Staubli, 1983; Gopalkrishnan, 1993; Spencer et al., 2007). This type of VIV experiment allows the amplitude and frequency of cylinder vibration to be altered to obtain corresponding hydrodynamic forces experienced by the cylinder. Sarpkaya (1978) was one of the earliest to conduct such experiments. Through forced vibration experiments at Re range of 6000 to 35000, Sarpkaya reported that the maximum amplitude of cross flow vibrations was 0.9 diameter. Both in-phase and out-of-phase components of forces were reported as functions of amplitude ratio (A/D).

Staubli (1983) conducted forced experiments on elastically mounted cylinders at a Reynolds number range of 20,000 - 300,000 and showed the advantages of these experiments in which the amplitude and frequency values can be varied to obtain the corresponding lift and drag forces. Staubli observed that hysteresis effects are due to the nonlinear relation between the fluid force and oscillation amplitude.

From forced experiments, experimenters can obtain surface plots of lift (C_{LV}), drag (C_D) and added mass (C_M) coefficients as functions of amplitude ratio (A^*) and

reduced velocities (V_R).

$$A^* = \frac{A}{D} \quad (2.1)$$

$$V_R = \frac{U}{Df_o} \quad (2.2)$$

where A is the amplitude of forced oscillation, D is the cylinder diameter, U is free stream velocity, and f_o is the frequency of oscillation. Although forced experiments provide useful data for relating hydrodynamic forces to amplitude and frequency of vibrations, they are a time consuming way of obtaining such data. For each cylinder, strake, or fairing configuration, a large test matrix of experimental runs need to be carried out in order to obtain these VIV force coefficient plots.

Free Vibrations

Unlike forced vibration experiments, free vibration experiments are conducted on a finite length of a cylinder in which the cylinder is free to vibrate due to vortex shedding. This is a more realistic representation of VIV in an experiment setting. From free vibration experiments, one can typically obtain A^* versus U^* plot, correlation data, and cylinder motion.

$$U^* = \frac{U}{Df_n} \quad (2.3)$$

where U^* and f_n is reduced velocity for free vibration experiments and natural frequency of the cylinder segment, respectively. The reduced velocity in free vibrations is a function of natural frequency of the structure, which is different from the reduced velocity in forced experiments (Spencer, 2009). The reduced velocity versus amplitude ratio plots are useful for validating VIV numerical algorithms that use forced experimental data.

Laboratory Scale

Riser VIV experiments are also conducted on reduced scale risers (Li, 2005;

Chaplin et al., 2005a) in a laboratory setting and use the measured responses to make a prediction of the full scale responses. However, riser responses are extremely sensitive to Reynolds number and the number of modes along the riser. The reduction in scale will automatically change the Reynolds number, and also the number of modes to be present along the length. One approach is to increase the scale, but this means a considerable large facility (tank) will be needed. Therefore, this approach is not practical for deepwater risers. These types of experiments are useful for validating numerical models, especially in the capturing of multi-modal vibrations along the spanwise direction.

Large scale tests

The most expensive VIV experiments are those conducted in lakes or oceans with large scale risers. This has been traditionally conducted as part of a joint industry project (JIP) which involves a number of organizations or companies with a common goal to address current industry issues, such as VIV prediction. This type of test represents the most realistic test conditions. However, realistic test conditions come with increased technical challenges. For instance, the measurement of current velocities require the calibration and installation of a large number of instrumentations along the riser. In addition, the current velocities cannot be controlled in the ocean. Therefore, the tests are usually conducted in calm water conditions, and the cylinders or pipes are first assembled to the desired configuration and towed through water at a desired speed to simulate current flow.

Vandiver (1983) conducted one of the first large scale cylinder tests in the lake of Castine, Maine in 1975 and 1976. These cylinders were 75-ft synthetic fiber or wire cables with diameters ranging from 0.64 to 1.59 cm. The current velocities in the tests were spatially uniform and varied with time, from 0.152 to 0.162 m/s. The vibration responses, as observed in these tests, were mostly single-mode lock-in vibration with amplitudes of one diameter. Low-amplitude random vibration responses were also observed. One of the most important observations was made when a 900 feet wire rope

of 0.71 cm in diameter was subjected to a mildly sheared current. Lock-in vibration with amplitudes of 0.5-1 diameter took place at the 50th mode. This confirmed that lock-in behaviour is possible for flexible pipes at high modes.

Jong and Vandiver (1983) and Vandiver (1983) conducted a 6-week experiment at the same site in Castine, Maine. Both cable (3.18 cm in diameter) and steel pipes (4.18 cm in diameter) of lengths 22.86 meters were used in this experiment. The tension, acceleration, mean drag coefficient, and current were measured. The primary goals of the tests were to determine the difference in the behaviour of cables and steel pipes (of different mass ratio and bending stiffness) and to measure and compare mean drag coefficients with those collected from laboratory experiments. The drag coefficients were shown to be high and oscillate with larger amplitudes over 2.5 hours of data for the steel pipe and oscillate less over time for the cable. This finding concluded that the mass ratio is important for understanding VIV. The mass ratio is defined as $\pi/4$ times the ratio of the cylinder mass per unit length over the mass per unit length of the fluid it displaces. The lower mass ratio cylinders have a broader range of lock-in behaviour than the higher mass ratio (Vandiver, 1993).

Large scale experiments are also used to validate numerical prediction models. For instance, Grant et al. (2000) conducted a field test in the Phase 1 Highly Compliant Riser (HCR) JIP. The test programme consisted of three different riser configurations: compliant vertical access riser (CVAR), SCR, and lazy wave SCR. A mechanical actuator is installed to simulate dynamic vessel heave motion, and significant intermittent VIV was observed. The data collected from these tests were used as benchmark validation study for a time-domain VIV prediction model developed by Grant et al. (2000).

Another recent large scale VIV experiment took place offshore Miami in 2006. This Gulf Stream test aimed to collect high mode VIV response data on a densely instrumented cylinder, conduct partial and full coverage of strakes and fairings on cylinders, and estimate drag forces on cylinders with and without strakes and fairings.

The test was conducted with a composite pipe with an outer diameter of 1.43 inches and a length of 500.4 feet. These dimensions were chosen in order to obtain more than 10 modes of vibrations. The pipe was connected to a research vessel at the top and a railroad wheel (weighing 805 pounds in air) at the bottom to provide tension. This set up simulates a tensioned beam with pinned-pinned end boundary conditions. Fiber optic strain gauges were installed to measure the vibration responses. One interesting finding was the occurrences of higher harmonics that are not orthogonal to the crossflow and inline direction. In addition, structural responses were observed to contain the form of wave propagation (Marcollo et al., 2007).

Murrin et al. (2007) conducted a high mode VIV experiment on a large-scale riser that was towed off the east coast of Newfoundland, in The Cordelia Deep. The riser was 130 meters in length, with an outer diameter of 53mm and an inner diameter of 40mm. The large scale riser was towed at speeds ranging from 0.15 to 1.25 m/s. For each run, the data was recorded by the accelerometers for 3 minutes after the vessel speed has reached steady state. The data was analyzed and to obtain acceleration, displacement and the frequencies of motion. The results of multi-modal vibrations from this experiment have not yet been published in the public domain.

Chapter 3

Time-Domain Model

3.1 General

The model being adopted uses empirical hydrodynamic VIV coefficients from forced experiments and formulates the problem in the time-domain. As part of the JIP-Deepstar project, a large database of hydrodynamic VIV coefficients was collected on finite segments of risers and risers with suppression devices. These data sets come from forced experiments in which the cylinder (or riser segment) is towed through water at a constant speed while being subjected to oscillation at a specified amplitude and frequency (Spencer et al., 2007).

Most forced VIV experiments conducted in the past are for relatively low Reynolds number flows. This limitation can be one of the factors influencing the accuracy of VIV predictions. The forced VIV experimental setup shown in Figure 3-1, however, is equipped to conduct forced experiments for high Reynolds number flows (up to 1.8×10^6). The increase in Re makes the collected hydrodynamic coefficients more valid for realistic applications. In order to utilize these coefficients for longer risers, a numerical model is to be developed in this work. This chapter will give a detailed description of the numerical model being developed and the rationale for such a model.

3.2 OCC's Forced Experiments

Spencer et al. (2007) have collected forced VIV coefficients on cylinders using the high Reynolds number VIV test apparatus at Oceanic Consulting Corporation (OCC). The setup of these experiments is shown in Figure 3-1. In these forced experiments, cylinders are forced to oscillate at a prescribed frequency and amplitude while being towed through water.

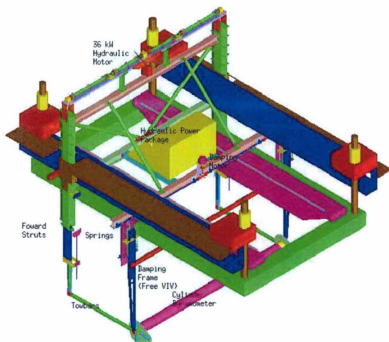


Figure 3-1: Oceanic Consulting Corporation's VIV test apparatus

The measured hydrodynamic forces acting on the cylinder are decomposed into two components, lift and drag, acting at 90 degrees to each other. The oscillation occurs in the lift direction (cross-flow); the lift force is therefore further decomposed

into two components, one in phase with velocity and the other in phase with acceleration (added mass). The lift component that is in phase with velocity tends to excite or dampen the vibration in the cross-flow direction. The lift component that is in phase with acceleration alters the apparent mass of the cylinder. Further processing of the collected data will give force coefficient (lift, drag and added mass) curves that are dependent on non-dimensionalized velocity (reduced velocity) and amplitude of oscillation (amplitude ratio). Forced oscillation experiment data from the Deepstar funded project (Spencer et al., 2007) have been utilized in this research.

The database of coefficients used in the present model includes added mass, drag, and lift coefficients that depend on the amplitude ratio (A^*) and reduced velocities (V_R) from the forced experiments. This database of coefficients was collected on a bare cylinder without VIV suppression devices.

The drag coefficient is regarded as the hydrodynamic force in the inline direction. This force has a steady and oscillating component as defined in the following Section.

The added mass is applied to the crossflow direction as this was derived from the lift forces that were in phase with acceleration. The added mass changes the apparent mass of the riser and subsequently alters natural frequency of the system. In this present database, the added mass (C_M) coefficients can be both positive or negative. Positive C_M means an increase in apparent mass and a decrease in natural period (Spencer et al., 2007).

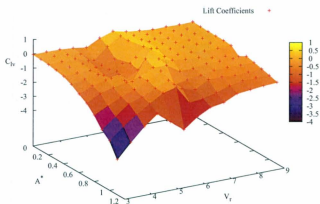


Figure 3-2: Lift Force Coefficients

The lift coefficients (C_{LV}), in phase with velocity, are plotted against A^* and V_R and shown in Figures 3-2 and 3-4. In these figures, C_{LV} shows both negative and positive values. Positive C_{LV} means energy is being put in the system to excite vibration, and negative C_{LV} represents energy removed from the system and the vibration is damped. In other words, both hydrodynamic excitation and damping are included in the C_{LV} database. This is different from programs such as Shear7, in which separate models are implemented for excitation and damping.

Figure 3-3 shows the Venugopal damping model that is used in Shear7. In the Venugopal model, damping is defined for reduced velocities less than 5 and greater than 8. Excitation is assumed to occur at reduced velocities in the range of 5 and 8, and a separate model is implemented for this.

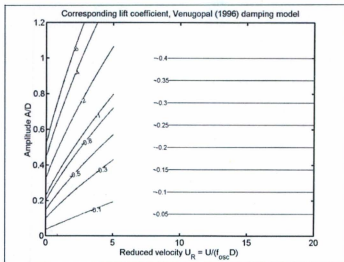


Figure 3-3: Venugopal Damping Model for Low and High Reduced Velocities

As noted in the work of Spencer et al. (2007), Figures 3-2 and 3-4 in the present database show similarity in lift coefficients between Venugopal's damping model at low and high reduced velocity where most of the damping occurred. At low reduced velocities and high amplitude ratio, the plot shows a steep decrease in C_{LV} values. At higher reduced velocities, it is shown on the surface plot that the C_{LV} values are nearly constant. However, there is a "well" in Figure 3-4, showing negative C_{LV} values between reduced velocities of 4.5 to 5.5 with amplitude ratios less than 0.6. This is not captured in the Venugopal damping model.

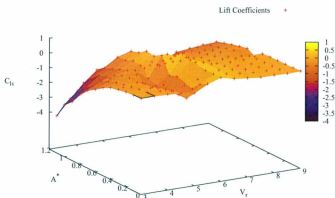


Figure 3-4: Lift Force Coefficients (Rotated View)

A new approach was developed in the work of Spencer et al. (2007) to make full use of the available high Reynolds number VIV coefficients. In their work, hydrodynamic damping was included as an extension of the lift coefficient curves. The VIV forcing algorithm adopted in this work is based on their work. The algorithm was then implemented with a global-coordinated-based finite element program to analyze VIV on longer risers.

3.3 Time-Domain Forcing Algorithm

In the Deepstar test programme, forced experiments with both single frequency and two frequency components combined were conducted. The latter type includes the combination of two frequencies such that the signals beat together and the amplitude varies continuously. It was shown that the lift force and added mass measured from one unsteady cycle with amplitude, A and frequency, f was similar to those found with multiple cycles of constant period and amplitude. This implies that the fluid

particles have no memory of their path, and that only the current state variables (A^* , V_R) of the cylinder play a role in the loads experienced by the cylinder (Spencer et al., 2007). With this in mind, it is possible to use the state variables of the previous cycle to estimate the forces on a cylinder in the next cycle, assuming that the cylinder motion does not change drastically from one cycle to the next. This forms the basis of the time-domain forcing algorithm in this work. The current state variables of the cylinder are determined from the responses of the previous cycle, and the algorithm uses these current state variables to interpolate along the hydrodynamic coefficient curves to determine force coefficients to be used in the next cycle.

Zero crossing analysis of the cross flow velocity is used to determine the period (T_0) and subsequently the amplitude of the motion from the previous cycle. The determined amplitude and frequency, along with flow speed, are entered in Equation 3.1 and 3.2 to find the state variables (A^* , V_R).

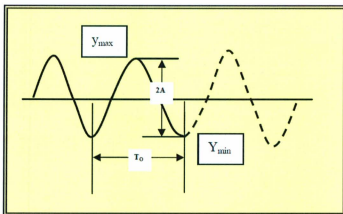


Figure 3-5: Zero Crossing Analysis of a Vibration Cycle (from Spencer et al., 2007)

$$A^* = \frac{y_{max} - y_{min}}{2D} \quad (3.1)$$

$$V_R = \frac{UT_0}{D} \quad (3.2)$$

The definitions of y_{max} , y_{min} , and T_0 are shown in Figure 3-5. The computed state variables are then utilized to interpolate along the surface curves of lift (C_{LV}), added mass (C_M), and drag (C_D) coefficients. The interpolation of these coefficients are described in Section 3.3.1. The interpolated values are utilized as hydrodynamic force coefficients for the next cycle.

Transverse Force

The total transverse force consists of two force components that are in phase with acceleration and velocity. The component that is in phase with velocity is from the lift (C_{LV}) coefficient in which either excitation or damping is applied depending on the sign of the interpolated C_{LV} values. The component that is in phase with acceleration is from the added mass (C_M) coefficient. The total transverse force $L(t)$ at each time step is given by

$$L(t) = \frac{1}{2}C_{LV}(A^*, V_R)\rho LDV^2 \sin[\omega(t - t_0)] + \frac{\pi}{4}C_M(A^*, V_R)D^2\rho L\omega^2 A^* \cos[\omega(t - t_0)] \quad (3.3)$$

where $\omega = \frac{2\pi}{T}$ and V is the transverse component of relative velocity. The lift force is synchronized to the cylinder velocity by re-starting the lift at the point where the last cycle ended and the crossflow velocity was zero.

Inline Force

The total inline force in the present model is computed from the drag force coefficient, as shown below.

$$C_D(t) = C_{D0} + [C_D(A^*, V_R) - C_{D0}] \sin[2\omega(t - t_0)] \quad (3.4)$$

where $D(t)$ is total time-varying drag coefficient. The drag force has a steady

component (C_{D0}) as well as an oscillating component. The measured drag coefficient (C_D) is subtracted from the steady component to obtain the oscillating component as shown in Equation 3.4. The drag oscillation takes place at twice the frequency of the lift oscillation.

Structural Damping and Correlation Length

Structural damping is relatively small compared to hydrodynamic damping in deepwater applications. Therefore, the structural damping is ignored in this model, but can be included as a percentage of the total damping force.

No assumption is made on the correlation length in this model. The response of each element in the present model is dependent on its current state variables, and the correlation between adjacent elements is implicitly included in the structural response. This should be valid for the time-domain solution, as the response is updated at each time step.

3.3.1 Surface Interpolation

Two approaches were taken to interpolate the force coefficient curves based on the current state variables (A^* , V_R) of the cylinder. The first method was utilizing a subroutine, DSURF, from the IMSL math library. DSURF is an interpolation subroutine for scattered data. The algorithm uses Akima's surface fitting method, and is locally of fifth order in two variables. Due to the structure of the collected experimental data, this interpolation method was not valid for areas near the corners and whenever there was a sharp change in state variables.

A new interpolation subroutine was needed that could be tailored to this database of coefficients. After searching for various high order methods and evaluating the pros and cons of each, it was decided to use bilinear interpolation for these surface curves. In this approach, the force surface curves are first discretized into smaller rectangular grids with A^* as independent variable in one direction, and V_R as the other independent variable.

Once the current state variables (A^* , V_R) are found through zero crossing analysis, a search algorithm begins to find the grid (on the force coefficient curves) in which these two state variables lie. Once the grid is found, bilinear interpolation is conducted on the surface of the grid to determine the force coefficients (C_{LV} , C_D , and C_M) through interpolation.

The interpolation on the grid (or panel) requires the use of interpolation functions to describe the domain. These interpolation functions are taken from the theory of finite element. In the finite element formulation, the interpolation functions used to describe a surface on the domain $[-1, 1]$ are

$$N_1(\xi, \eta) = \frac{1}{4}(1 - \xi)(1 - \eta) \quad (3.5)$$

$$N_2(\xi, \eta) = \frac{1}{4}(1 + \xi)(1 - \eta) \quad (3.6)$$

$$N_3(\xi, \eta) = \frac{1}{4}(1 + \xi)(1 + \eta) \quad (3.7)$$

$$N_4(\xi, \eta) = \frac{1}{4}(1 - \xi)(1 + \eta) \quad (3.8)$$

In order to use this on a more general domain, something other than $[-1, 1]$ in ξ and η , the following generalized shape functions may be adopted,

$$N_1(\xi, \eta) = \frac{1}{c}(d_1 - \xi)(d_3 - \eta) \quad (3.9)$$

$$N_2(\xi, \eta) = \frac{1}{c}(d_2 + \xi)(d_3 - \eta) \quad (3.10)$$

$$N_3(\xi, \eta) = \frac{1}{c}(d_2 + \xi)(d_4 + \eta) \quad (3.11)$$

$$N_4(\xi, \eta) = \frac{1}{c}(d_1 - \xi)(d_4 + \eta) \quad (3.12)$$

where $c = (d_1 + d_2)(d_3 + d_4)$. The local coordinate system of the grids and the distances d_1 , d_2 , d_3 , d_4 are shown in Figure 3-6.

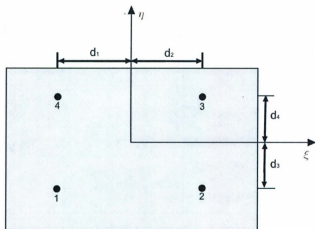


Figure 3-6: Interpolation grid

If the grids are connected by equally spaced nodes in each of their independent axis, then $d_3 = d_4$ and $d_1 = d_2$. Also note that if the domain is $[-1,1]$ in both ξ and η , then Equations 3.9 - 3.12 are reduced to Equations 3.5 - 3.8.

According to Beer et al. (2008), the interpolated values of C_{LV} , C_D or C_M within any quadrilateral (or rectangular) domain is given as

$$C_{LV} = N_1(\xi, \eta)C_{LV}(1) + N_2(\xi, \eta)C_{LV}(2) + N_3(\xi, \eta)C_{LV}(3) + N_4(\xi, \eta)C_{LV}(4) \quad (3.13)$$

Replacing C_{LV} with either C_D or C_M in Equation 3.13 gives the interpolation for drag and added mass coefficients, respectively. Once the coefficients are found, they are used in the computation of hydrodynamic loads, as shown in the chapter of Mathematical Formulation in Appendix A.

3.3.2 Current Profile

Current flow is the most important factor in determining whether VIV will take place. The current speed determines the vortex shedding frequency and controls whether or not lock-in will occur. It is desirable to have a model that can manage various current profiles. In an attempt to satisfy this, effort was taken to implement various current profile capabilities in the present model.

At present, the model can take three different types of current profiles as shown in Figure 3-7.

1. Uniform current with constant direction
2. Sheared current with constant direction
3. Arbitrary current with arbitrary direction along the water depth

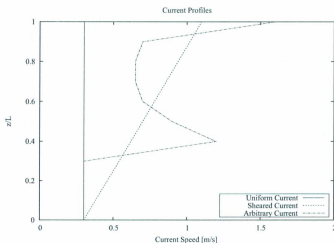


Figure 3-7: Current profiles available in the present model

The uniform current profile requires the input of two values (current speed and direction). The model then distributes this along the entire depth of the water column.

The sheared profile requires the input of the current at the top (usually the higher value), the current at the bottom (usually the lower value), and a constant current direction. The model assumes a linear relationship between the current and the depth, and automatically computes the current distribution along the depth.

The above current profiles were implemented to ease simulation for research studies. Research on VIV is mainly carried out in uniform or sheared current profiles. This, however, is never the case in practical applications. The third current profile requires the user to input n points (Z , current velocity, phase angle) along the water column, starting from the top at $Z = 0$. The present model assumes a linear distribution between the user input points.

The Z location of each element is first computed, and the program linearly interpolates the current profile to evaluate the current speed that the element is subjected to. This, along with the motion of each element, is then utilized to compute the relative velocity of the riser-fluid interaction. This computation is described in further detailed in Appendix A.

3.4 Finite Element Methods

The finite element method (FEM) is a numerical method for solving the behaviour of a continuum by dividing it into a finite number of elements that are functionally interrelated. This is accomplished by transforming the governing differential equation into a system of algebraic equations. The discretized elements are connected by nodes at the interfaces and each element must satisfy compatibility, stress equilibrium and boundary conditions through piecewise approximation over the domain.

The FEM is the most general method for analyzing the behavior of slender structures, such as mooring lines and risers, in the offshore industry. The FEM is an attractive method because it offers a wide variety of elements to model the most complex mooring or riser systems. Beam elements have been traditionally adopted for

the modeling of risers with an updated Lagrangian approach to account for geometry nonlinearity.

Nordgren (1974) derived the nonlinear equations of motion based on the theory of rods. In his work, the motion of three-dimensional inextensible elastic rods with equal principal stiffness were solved using the finite difference method. This set of equations of motion was solved later in the work of Garrett (1982) using the finite element method. In his work, Garrett utilized a global coordinate based formulation to take advantage of the slender nature of rods. This approach reduced the computation requirement since the global coordinate based approach does not require the computation of coordinate transformation. Yin and Qiu (2007) utilized this approach for the static and dynamic analysis of mooring lines, forming the program MAPS-Mooring. This work is aimed at validating MAPS-Mooring and then extending the program to include the capability of VIV analysis.

3.5 Summary of VIV Algorithm

As stated in Section 2.1, the important parameters affecting the accuracy of VIV prediction models are: current profile, excitation and correlation length of lift forces and vortex shedding, frequency and magnitude of the lift force exerted on the riser as a result of vortex shedding, hydrodynamic damping, and riser structural properties or geometry. This section will provide a summary on how each of these are implemented in the present model.

One of the strengths of the time-domain model is the capability of accounting for nonlinear boundary conditions and loads. In the present model, the current profile can be uniform, sheared, and arbitrary. The arbitrary current profile option allows the user to input 21 different current speeds and angles along the water column. This is suitable for analyzing VIV for deepwater risers where varying current speeds are present along the water column.

Hydrodynamic damping is included as part of the lift force that depends on the state variables (A^* , V_R) of the system. Unlike traditional VIV models, where a separate damping model is used along with VIV forcing, the empirical lift coefficient database in the current model includes both damping and exciting forces. In other words, no assumptions are made on hydrodynamic damping in the current model.

The material properties of the riser are captured using a finite element model. Nonlinear rod element theory is utilized to describe the behaviour of the elements that compose the riser.

The correlation length is implicitly described using the finite element method. As the model operates in the time-domain, the correlation length should not be a concern as the applied VIV forces (excitation and damping) are dependent on the motion parameters of the riser. The results from the present VIV model are shown in Chapter 5.

Chapter 4

MAPS-Mooring Validations

This chapter presents the validation of the code, MAPS-Mooring developed in the work of Yin and Qiu (2007), for mooring lines in which VIV is not considered. The study was aimed to validate the finite element formulation by its application to the static and dynamic analyses of mooring lines. A summary of the theoretical background and numerical aspects of MAPS-Mooring is given in Appendices A and B.

4.1 Catenary Mooring Line Excursion

The first validation case conducted was a catenary mooring line, to which an analytical solution exists for the static problem. The mooring line was assumed to be inextensible. The characteristics of the mooring line are listed in Table 4.1.

Table 4.1: Parameters of a Catenary Mooring Line

Parameter	Value
Water Depth [m]	900
Water Density [te/m^3]	1000
Unit wet weight [kN/m]	0.2943
Unit mass [te/m]	0.0345
Diameter [m]	0.0390
Line Length [m]	1580.0
No. of Lines	1

The initial tension was taken to be zero, since it has no effect on the top tension of a catenary line. The axial stiffness (EA) was assumed to be extremely large, in order to simulate the inextensible line. The 1580-meter catenary line was discretized into 100 and 300 elements, and MAPS-Mooring Static Analysis was utilized to compute the static top tension of the line. For each computation, the fairlead point was fixed and the anchor point was moved along the x-axis to obtain the static load-excursion curve, as shown in Figure 4-1.

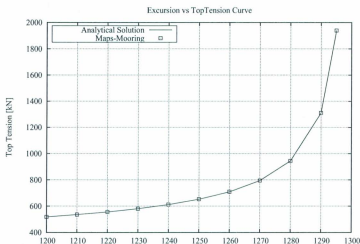


Figure 4-1: Top Tension Comparison of a Catenary Mooring Line

The analytical solution was obtained using classical catenary equations, as shown below:

$$s = c \tan(\theta)$$

$$x = c \sinh^{-1} \left(\frac{L}{C} \right)$$

$$y = c \left[\sqrt{1 + \left(\frac{wL}{H} \right)^2} - 1 \right]$$

Figure 4-1 shows the static top tension vs line excursion between MAPS-Mooring outputs (100 elements) and the calculated analytical solution. The computed results showed good agreement with analytical solution. In addition, there was almost no

discrepancy between the computed results of 100 elements and 300 elements from MAPS-Mooring.

4.2 Catenary Mooring Line Subjected to an Anchor Force

The next case is a catenary mooring line subjected to a horizontal force at the anchor. This case was presented in Yin and Qiu (2007) and was regenerated in this study. The total line length utilized in the study was 160 meters, the unit weight was 0.4 kN/m, while subjected to a horizontal force of -64, -32, -12.8, or -6.4 kN (to simulate WL/T values of 1, 2, 5, and 10 respectively). Again, the axial stiffness (EA) value was chosen to be very large to ensure the line was inextensible. The computed results were post-processed and compared with the analytical results. The X/L value was obtained by dividing the absolute values of the x-coordinate of the anchor by the total length (160), and the same manipulation was done to obtain Y/L . The α value can be calculated using the tangent vectors (x' and z') at the fairlead point and basic trigonometry. The post-processed results are presented in Table 4.2.

Table 4.2: Results for Catenary Line subjected to horizontal anchor force

	α (deg)	X/L	Y/L
WL/T	1		
1 Element	45.374	0.88138	0.41426
10 Elements	45.000	0.88137	0.41421
Analytical	45.000	0.88137	0.41421
WL/T	2		
1 Element	63.277	0.72194	0.6179
10 Elements	63.434	0.72182	0.61803
Analytical	63.435	0.72182	0.61803
WL/T	5		
1 Element	75.705	0.46756	0.82216
10 Elements	78.689	0.46249	0.81981
Analytical	78.690	0.46249	0.8198
WL/T	10		
1 Element	80.720	0.30168	0.92065
10 Elements	84.289	0.29982	0.90499
Analytical	84.289	0.29982	0.90499

As can be seen from the above, the computed results showed a perfect agreement when 10 or more elements were adopted to model the 160-meter catenary line. This further shows the robustness of the static analysis algorithm of MAPS-Mooring.

4.3 Forced Oscillation Experiment

Following the development of a finite element algorithm for mooring line analysis, Faure (1989) conducted a set of experiments to validate the algorithm. One of the experiments was a forced oscillation test, from which the published data was utilized

to compare with the outputs from MAPS-Mooring's Dynamic Analysis.

The characteristics of the mooring line are listed below. Oscillatory motion was applied at the top end of the line while it was being suspended in still water. The Oscillatory motion was generated by a mechanical actuator that moved the top end of the line back and forth along the x-direction, producing a harmonic top end excitation. One of the tests was conducted with a motion amplitude of 0.15 meter at a frequency of 0.49 Hz.

Table 4.3: Parameters used in Faure's Forced Oscillation Experiment

Parameters	Values
Water Depth [m]	1.73
Water Density [te/m^3]	1000
Initial Tension [kN]	0.0121
Drag Coefficient (Normal)	1
Drag Coefficient (Tangential)	0.1
Inertial Coefficient	1
EA [kN]	62.8
EI [$kN\cdot m^2$]	1.97E-04
Unit wet weight [kN/m]	8.88E-04
Unit mass [te/m]	9.05E-05
Diameter [m]	3.80E-03
Line Length [m]	1.64E+01
No. of Lines	1

The dynamic analysis was then carried out in MAPS-Mooring using the model information listed in Table 4.3. Prior to the dynamic analysis, the static configurations of the mooring line was first determined. The fairlead coordinate of the mooring line was chosen to be at the origin, the anchor coordinates were then guessed and checked until the top tension computed by MAPS-Mooring matched closely with the pretension listed above. During that process, if the computed static top tension was less than the pretension - then the anchor point was moved further away from the fairlead along the direction of the line; else the anchor point was moved closer.

With the equilibrium positions of the mooring line determined, the dynamic

analysis was then carried out. To ensure numerical stability, a time step of 0.001 second was used. The computation was carried out for 15 seconds. The time series of the computed top tension at four time steps is shown below.

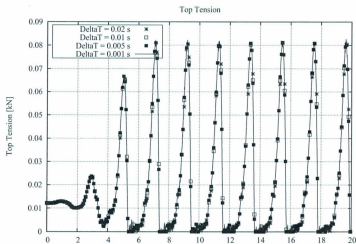


Figure 4-2: Top Tension Time Series for 0.15 forced motion amplitude at 0.48 Hz

This time series is characterized by two regions. The first five seconds of plot may be explained by the transient response of the mooring line under harmonic forced oscillation. After the five second mark, the mooring line reaches a steady response and the top tension oscillates in accordance with the forced motion.

Faure presented the experimental measured tension to be oscillating between 89 Newtons and 0 Newtons at a period of approximately 2 seconds. Figure 4-2 shows the computed tension from MAPS-Mooring. The computed tension was oscillating between approximately 81 Newtons to 0 Newtons at a period of about 2 seconds. The discrepancy is about 9%, which is acceptable for nonlinear time-domain analysis. The discrepancy may result from bottom boundary conditions.

4.4 Comparison with Full Scale Experiment

Ormberg et al. (1983) conducted full scale experiments onboard the SSV Henrik Ibsen and the published data from this experiment was adopted to validate MAPS-Mooring dynamic analysis. The main inputs of the mooring system is presented in Table 4.4.

Table 4.4: Parameters of the mooring system onboard SSV Henrik Ibsen

Parameter	Value
Water Depth [m]	70
Water Density [te/m^3]	1
Drag Coefficient (Normal)	1.5
Drag Coefficient (Tangential)	0
Inertial Coefficient	1
EA [kN]	280937
EI [$kN\cdot m^2$]	1081
Unit wet weight [kN/m]	0.1926
Unit mass [te/m]	0.0226
Diameter [m]	0.7
Line Length [m]	1300

Based on the diameter of the mooring wire given, the stiffness and unit wet weight of the mooring line were interpolated using the equations presented in the work of Ma and Qiu (2010). The tensions in the lines were sampled once every second. Results from three samples were presented in the work of Ormberg (1983). The environmental condition, tangential motion, and measured tension variation are tabulated below.

Table 4.5: Environmental loads for Full Scale Experiment

Sample No.	Wind Speed[m/s]	Wave		Tang. Motion	
		Hs[m]	Tz[sec]	Avg.[m]	St.Dev.[m]
1	24	6.12	8.14	0	0.49
2	25-30	6.74	8.48	0	0.66
3	21	5.6	8.17	0	0.43

While MAPS-Mooring is capable of inputting external loads in the analysis, the wind force was not included in the computation since the projected area of the superstructure exposed to wind was not known. However, the wave and tangential motions were imposed on the mooring line. Convergence tests were first conducted to verify the stability of the program, and its sensitivity to the number of elements and time step using Sample 1 in Table 4.5.

First the analysis was done for a 26-element mooring line, then followed by 52 and 104 elements at a fixed time step of 0.01 seconds. The top tension at each time step is plotted for different element sizes and presented in Figure 4-3.

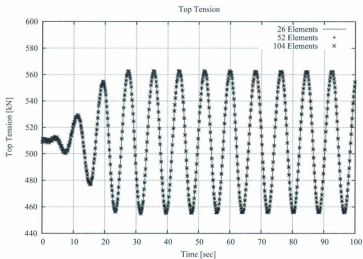


Figure 4-3: Sensitivity to No. of Elements

The convergence test is then carried out for the sensitivity of time step. Three different time steps, 0.1, 0.05, and 0.01 were used in this test at a fixed element of 52 elements. The results of the top tension are shown in Figure 4-4.

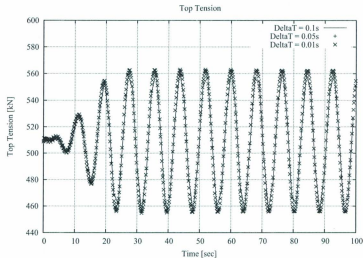


Figure 4-4: Sensitivity to time step

The convergence of the program is demonstrated with the three sets of elements and three time steps, as shown above. The top tensions for the other two samples are presented below.

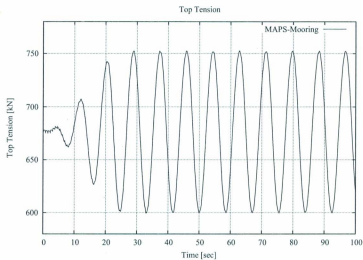


Figure 4-5: Top Tension for Sample 2

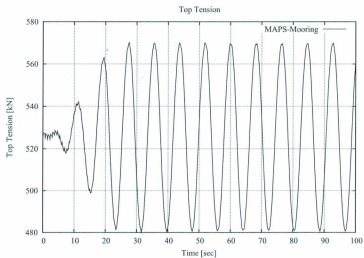


Figure 4-6: Top Tension for Sample 3

The comparison of the tension variation measured in the full scale experiment

is compared with the results computed by MAPS-Mooring. Table 4.6 shows the measured tension variation from the field experiment as well as the tension variation from MAPS-Mooring.

Table 4.6: Measured vs. MAPS-Mooring Tension

Sample No.	Avg. Tension [kN]	Tension Variation [kN]	
		Measured S.D.	MAPS-Mooring
1	498	70.6	65
2	675	100	77
3	525	57.8	45

The comparison showed that the tension variations computed by MAPS-Mooring were, in general, 20% lower than the measured values. This is due to the exclusion of the wind forces. It is reasonable to have 20% of the total tension due to the wind loads on superstructures. The wind acting on the offshore structure imposes motion on the top end of the mooring line. This imposed motion will cause a larger excitation at the top end of the mooring line and hence higher dynamic tension oscillation. However, this case should be re-computed if the projected area of the superstructure is known.

4.5 Comparison with Kitney and Brown's Experiment

Further validation of MAPS-Mooring Dynamic Analysis was conducted based on experimental data presented in the work of Kitney and Brown (2001). Both small and large scale model tests were conducted. The small scale test, conducted at a scale of 1:70, was carried out at the University College of London (UCL). The large scale test (1:16) was carried out at the Ship Dynamics Laboratory, Canal de Experiencias Hidrodinamicas de El Pardo (CEHIPAR) of Madrid, Spain. The characteristics of the full scale mooring line is shown in Table 4.7. The dynamic analysis was then carried in MAPS-Mooring based on these inputs.

Table 4.7: Full Scale Characteristics of Kitney and Brown's Experiment

Parameter	Value
Water Depth [m]	82.5
Line Length [m]	711
Diameter [m]	0.14
Unit Weight [kN/m]	3.202
Elastic Modulus [kN]	1.69E+06

The results of four different top-end motions, at non-dimensional motion amplitudes (a/d) 0.03, 0.05, 0.07 and 0.09, are presented in Figures 4-7 to 4-10, respectively.

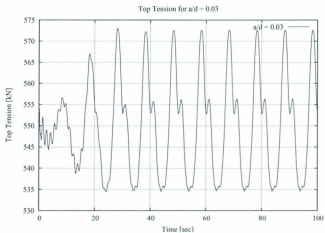


Figure 4-7: Top Tension for non-dimensional motion amplitude of 0.03

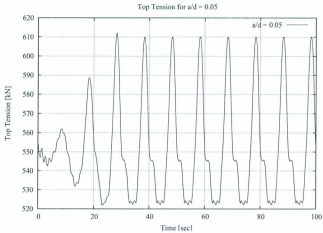


Figure 4-8: Top Tension for non-dimensional motion amplitude of 0.05

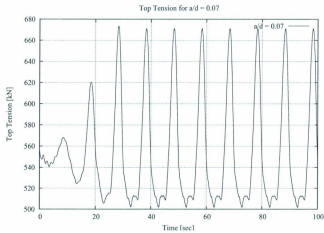


Figure 4-9: Top Tension for non-dimensional motion amplitude of 0.07

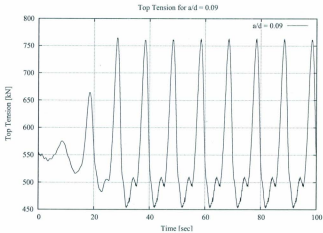


Figure 4-10: Top Tension for non-dimensional motion amplitude of 0.09

The dynamic tension was then non-dimensionalized and compared with the experimental results presented in the work of Kitney and Brown (2001). The non-dimensional dynamic tension is expressed as the ratio of dynamic tension to the static tension at the top of the mooring line.

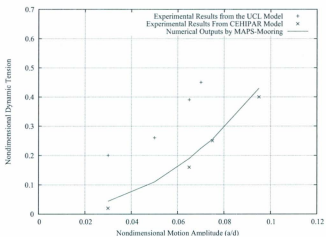


Figure 4-11: Comparison of non-dimensional dynamic tension

As can be seen from Figure 4-11, the results from MAPS-Mooring is in very good correlation with the experimental data obtained from the CEHIPAR (large scale) model. The smaller scale model from UCL showed higher non-dimensional dynamic tension than both MAPS-Mooring and the CEHIPAR model. This may be explained by the scaling effects on mooring lines. Scaling of mooring lines is challenging due to the large length-to-diameter ratio and nonlinear line properties. Therefore, data accuracy tends to decrease as model scale increases.

Chapter 5

MAPS-VIV Validation

5.1 Solid Cylinder VIV

Free vibration experiments were conducted on the same cylinder from which the forced VIV coefficients were obtained. As noted in the section of experiments, forced VIV is not “real” VIV. Realistic VIV is obtained from the so-called “free vibration” experiments. The goal of this study is to examine how well the new forcing algorithm reproduces the free VIV responses using forced VIV coefficients. The forcing algorithm is validated if the outputs match the free vibration data obtained on the same cylinder.

The parameters of the solid cylinder used in these two experiments are listed in Table 5.1.

Table 5.1: Solid Cylinder Properties

Parameters	Values
Diameter	0.325 m
Length	6.02 m
Mass	800 kg
Stiffness K	40000 N/m

The solid cylinder VIV was simulated using the forcing algorithm described in Section 3.3. The solid cylinder was connected to springs at both ends with an overall stiffness of 40 kN/m. The nondimensional cross flow displacement time series are shown for a number of uniform flows and shown in Figures 5-1 to 5-5. The nondimensional displacement time series is defined as the ratio of vibration displacement to the diameter of the cylinder. Figure 5-1 shows the results for a rigid cylinder subjected to a uniform flow of 1.1 m/s. At this speed, VIV does not develop for this cylinder. The initial transient vibration was damped out over a few seconds of simulation.

The results for the current speed of 1.6 m/s is shown in Figure 5-2. After the transient results, at approximately 20 seconds, the vibrations occur to be sinusoidal. This corresponds to the lock-in region. At $U = 1.6$, the nominal (U^*) and reduced (V_R) velocities are approximately 5.6. Given the same current velocity and pipe diameter, the same nominal and reduced velocities mean that the vibration frequency approaches the natural frequency of the cylinder; therefore lock-in was shown in the responses. In addition, Figure 5-3 shows the nondimensional responses of the cylinder subjected to a flow of 1.8 m/s. The corresponding V_R in this simulation (for the steady cycles) is approximately 5.7 while the nominal velocity is 6.3. As seen in the figure, the lock-in or sinusoidal trend is still seen in this simulation since the vibration frequency is close to the natural frequency of the system.

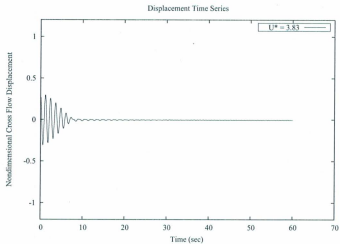


Figure 5-1: Rigid riser VIV for uniform current speed of 1.1 m/s

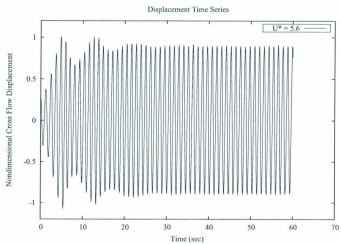


Figure 5-2: Rigid riser VIV for uniform current speed of 1.6 m/s

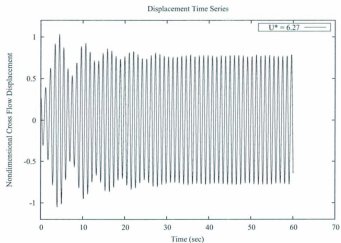


Figure 5-3: Rigid riser VIV for uniform current speed of 1.8 m/s

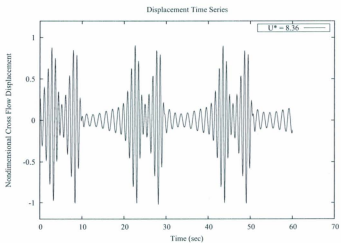


Figure 5-4: Rigid riser VIV for uniform current speed of 2.4 m/s

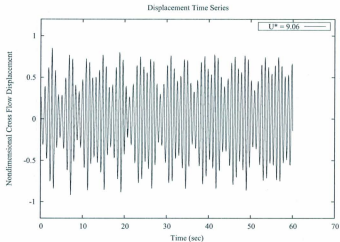


Figure 5-5: Rigid riser VIV for uniform current speed of 2.6 m/s

Figure 5-4 and 5-5 show the cross flow vibration of the cylinder subjected to higher flow velocities. Due to the self-limiting nature of VIV, the cross flow vibration is not as dominant in these simulations. Simulations were also carried out for a range of flow velocities. The results are post-processed, in the form of a generic free vibration plot, and shown in Figure 5-6. The nominal velocity (U^*) was obtained based on the current velocity, natural frequency of the rigid cylinder, and cylinder diameter. The amplitude ratio (A^*) corresponding to each nominal velocity was obtained by the root mean square of the crossflow vibration amplitudes over the simulation period. The computed results are compared with the experimental free vibration results obtained from the same cylinder.

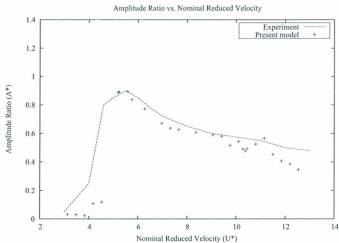


Figure 5-6: Amplitude Ratio vs Nominal Reduced Velocity

The comparison has shown that the new forcing function was able to make full use of the forced vibration coefficients to capture free VIV. The comparisons between the predicted and the measured free VIV are in good agreement.

5.2 Comparison with Chaplin's Experiments

5.2.1 General

A laboratory scale riser VIV experiment was conducted by Chaplin et al. (2005a) in the flume tank at the Delft Hydraulics Laboratory. A series of measurements were taken on a vertical riser subjected to a step current. The riser was tested with the lower 45% of it subjected to uniform current up to 1 m/s while the upper part was in still water. The responses of the system were measured at 32 equally spaced locations along its length. The properties of riser used in the experiment are shown in Table 5.2.

Table 5.2: Properties of the riser used in the Delft VIV experiment

Parameters	Value
Diameter	28 mm
Length	13.12 m
Length/Diameter ratio	469
Mass ratio (mass/displaced mass of water)	3
Submerged weight	12.1 N/m
Bending stiffness	29.9 Nm ²
Re range	2500 - 25000

Figure 5-7 shows the setup of the experiment. The test tank was 230m in length and 5m in width. The water depth was 6.5m for these tests. The lower part of the riser passes through the 6.5m water depth while the upper part was inside a vacuum tank. As the carriage moves, it simulates a step current with uniform speed on the lower part and no current on the upper part of the riser.

The riser was fixed with universal joints at each end. The top end was also connected to a tensioning system for tension adjustment. The results showed the displacements and curvatures at both ends were zero - confirming that both ends were fixed.

This setup was modelled using the numerical model developed in this research. The computational model is shown in Figure 5-8. The riser was fixed at both ends to simulate zero displacement and subjected to step current. The computation consisted of two steps: a static analysis to obtain the equilibrium profile of the riser, and subsequently followed by a dynamic analysis. The static analysis was also used to obtain the desired top tension, as reported in the experiment. This was done by moving the end condition (i.e. touchdown point) manually in the input file to obtain the desired top tension.

A total of four cases were simulated, corresponding to the current speeds and top

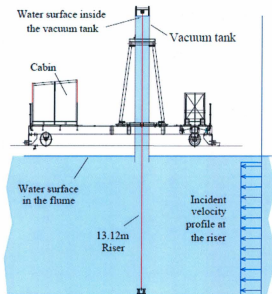


Figure 5-7: Delft VIV experimental setup

tensions shown in Table 5.3.

Table 5.3: Current speed and top tension of the Delft VIV experiments

Case	Current speed [m/s]	Top tension [N]
1	0.16	405
3	0.31	457
6	0.60	670
9	0.95	1002

In this study, the result of crossflow vibrations is plotted and presented here as vibration envelopes. These envelopes are the non-dimensionalized maximum and minimum vibration amplitudes of the riser. From the current model, vibration responses at each node are outputted to a standard text file. A Matlab program

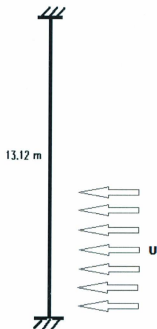


Figure 5-8: Computational Model of the Delft Experiment

was coded to retrieve the maximum and minimum amplitudes at each node over a pre-determined period of time and subsequently non-dimensionalized by dividing the diameter of the riser.

The convergence studies for the four cases are shown in the following sections. Results from the current simulation, physical experiment, Shear7 and Norsk Hydro are compared and conclusions are drawn. Norsk Hydro is a CFD-based program for riser VIV analysis. This program uses Navsim to perform the CFD computation on each plane and communicates with Usfos, a nonlinear structural code, to simulate VIV analysis.

5.2.2 Results for Case 1

The first case (Case 1) was for a step current with the lower 45% of the riser subjected to a current speed of 0.16m/s and an initial top tension of 405N. The first step in this study was to examine the convergence of element sizes. For a fixed time step of 0.0025 second, a convergence study was carried out for 50, 100, and 200 elements. Each simulation was conducted for a period of 250 seconds. The top tension of the riser was first plotted over the 250 seconds to determine the transient stage of the simulation. The transient results are then excluded from the analysis. Figure 5-9 shows the element sensitivity test for Case 1. As the number of elements increase from 50 to 200, it was shown that the results from 100 elements were similar to those from the 200 element simulation. Therefore, it was determined that 200 elements were sufficient in this simulation. This element convergence study also showed that a fixed time step of 0.0025 second was sufficient to reach convergence. Investigations were also carried out for other time steps (0.005 and 0.001), it was shown that the results from the 0.0025 did not differ much from the 0.001 time step. Therefore, a time step of 0.0025 was chosen for this study.

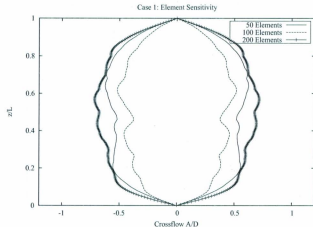


Figure 5-9: Case 1 Crossflow vibration envelope obtained from current model with 50, 100, 200 elements

The time series of crossflow vibration at the middle of the riser is shown in Figure 5-10 for the 200-element simulation. Crossflow vibration time series plots at other locations of the riser for this case are shown in Appendix C.

Comparisons were then made between the current model using 200 elements, experimental, Shear7 and Norsk Hydro results. The comparison is shown in Figure 5-11. Compared to the experimental results, the current model is shown to be able to predict the amplitudes of crossflow vibration. However, the experimental results showed sinusoidal envelope of vibration (mode shapes). The present model did not capture this, this may be due to the fact that the present model did not model correlation length. Correlation length is implicitly included in the structural response in the current model. However, the results from this simulation showed that the present model can predict better than the Norsk Hydro model. In addition, both the Norsk Hydro and the present model do not show sinusoidal shapes of maximum and minimum vibration along the length of the riser.

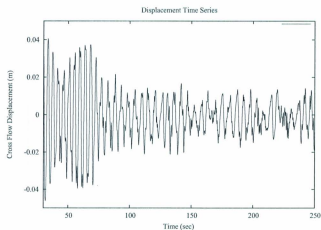


Figure 5-10: Case 1 Time Series of Crossflow Vibration at the middle of the riser

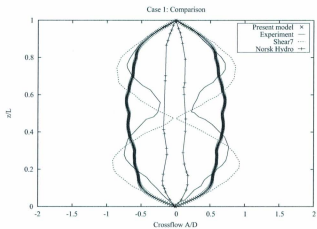


Figure 5-11: Case 1 Crossflow vibration envelope comparison between results from experiments, Shear7, Norsk Hydro, and the current model

5.2.3 Results for Case 3

The second case (Case 3 in Table 5.3) was for a step current of speed 0.31m/s and an initial top tension of 457N. The convergence study is shown in Figures 5-12 for 50, 100, and 200 elements at a time step of 0.0025 second. As shown in the figure, the results from all three simulations showed similar maximum and minimum crossflow vibrations. Therefore, 200 elements were shown to be sufficient for the analysis.

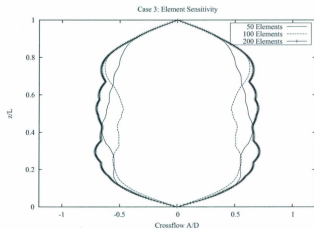


Figure 5-12: Case 3 Crossflow vibration envelope obtained from current model with 50, 100, 200 elements

The time series of crossflow vibration at the middle of the riser is shown in Figure 5-13 for the 200-element simulation. From this figure, it is shown that random vibration was observed over the 120-second simulation. Crossflow vibration time series plots at other locations of the riser for this case are shown in Appendix C.

The 200-element simulation results were then compared with the results from other models, as shown in 5-14. Similar to Case 1, the maximum and minimum amplitudes from the current simulation were in good agreement with the amplitudes from the experiment. However, the shapes of these maximum and minimum vibration

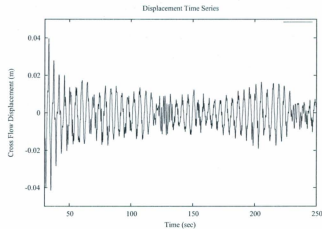


Figure 5-13: Case 3 Time Series of Crossflow Vibration at the middle of the riser

were not seen in the current model.

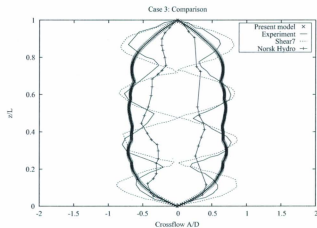


Figure 5-14: Case 3 Crossflow vibration envelope comparison between results from experiments, Shear7, Norsk Hydro, and the current model

5.2.4 Results for Case 6

The third case (Case 6 in Table 5.3) was for a step current of speed 0.6m/s and an initial top tension of 670N. The convergence study for this case is shown in Figure 5-15. The results for 50, 100, and 200 elements were shown to be close to one another, it was concluded that 200 elements were sufficient in this case.

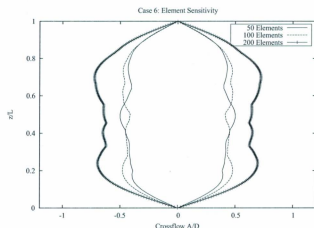


Figure 5-15: Case 6 Crossflow vibration envelope obtained from current model with 50, 100, 200 elements

The time series of crossflow vibration at the middle of the riser is shown in Figure 5-16 for the 200-element simulation. From this figure, it is shown that random vibration took place at this location over the entire simulation. Crossflow vibration time series plots at other locations of the riser for this case are shown in Appendix C.

The comparisons were made between the results from the current model with 200 elements, the experiment, Shear7, and Norsk Hydro. Figure 5-17 shows, once again, that the maximum and minimum amplitudes from the current model match well with those from the physical experiment.

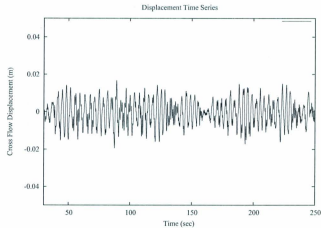


Figure 5-16: Case 6 Time Series of Crossflow Vibration at the middle of the riser

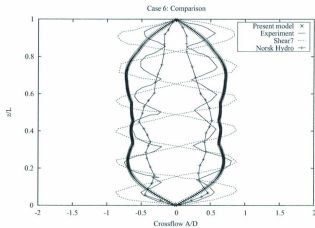


Figure 5-17: Case 6 Crossflow vibration envelope comparison between results from experiments, Shear7, Norsk Hydro, and the current model

5.2.5 Results for Case 9

The fourth case (Case 9 in Table 5.3) was for a step current of speed 0.95m/s and an initial top tension of 1002N. The convergence study is shown in Figure 5-18. As the number of elements increase, the amplitude envelope increases and approaches the amplitude envelope observed in the experiment. In addition, the time series of crossflow vibration at the middle of the riser is shown in Figure 5-19 for the 200-element simulation. From this figure, it is shown that lock-in occurred at this location with sinusoidal vibration over the 120-second simulation at an amplitude of approximately 0.021 meters. Crossflow vibration time series plots at other locations of the riser are shown in Appendix C.

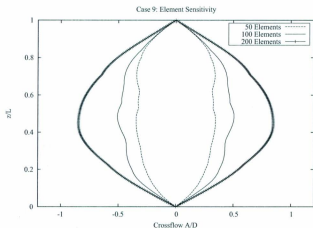


Figure 5-18: Case 9 Crossflow vibration envelope obtained from current model with 50, 100, 200 elements

The comparison between the models is shown in Figure 5-20 for Case 9. Like all other models, the present model underpredicts the amplitudes of vibration when compared with the experimental results. One explanation for this is the presence of a small systematic error during the experiment. A loose ball joint at the top or bottom

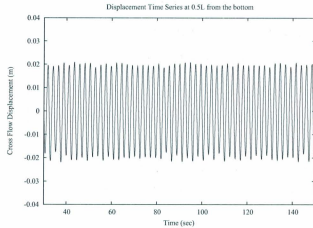


Figure 5-19: Case 9 Time Series of Crossflow Vibration at the middle of the riser

of the riser results in a decrease in the stiffness of the system. This decrease in system stiffness allows for higher vibration amplitudes, as reported in the experimental results by Chaplin et al. (2005b).

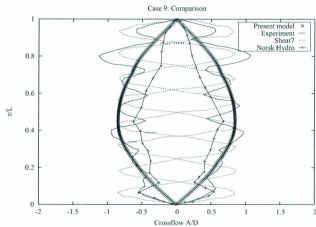


Figure 5-20: Case 9 Crossflow vibration envelope comparison between results from experiments, Shear7, Norsk Hydro, and the current model

5.2.6 Summary

The maximum and minimum crossflow vibration amplitudes (A/D) are shown in Figures 5-21 and 5-22 across the four models.

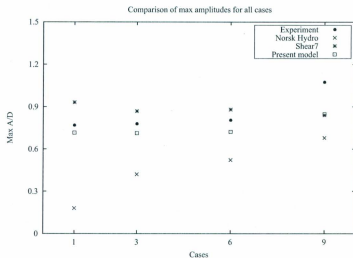


Figure 5-21: Max crossflow vibration across all models

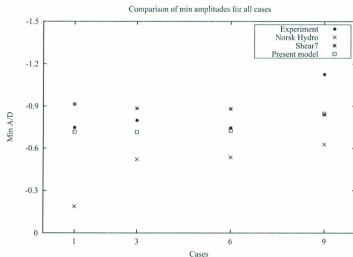


Figure 5-22: Min crossflow vibration across all models

There are a number of observations that were seen from the comparison across these models.

- There is a large scatter in the crossflow vibration across all models
- The Norsk Hydro model significantly underpredicts the responses
- Shear7 overpredicts the responses in all cases besides Case 9
- The maximum and minimum amplitudes in cases 1, 3, and 6 were in good agreement between the experimental results and the results from the present model
- These amplitudes predicted by the present method were lower in case 9 than the experimental ones. This case is characterized by a higher pre-tension. This could be due to an experimental error in which a loose connection at either end can result in larger-than-expected vibration amplitudes. Tensioning the riser

changes its natural frequencies (i.e. stiffness of the system), and increase in tensioning reduces overall vibration.

- The overall comparison showed that the present model predicted the maximum and minimum amplitudes better than Shear 7 in all cases. The present model also showed better agreement with the experimental results than Norsk Hydro did.
- The shape of the vibration envelope along the length of the riser was not clearly captured in this model. This may be caused by the method that was used to post-process the program outputs. It is evident from the results that both standing and travelling waves were present along the length of the riser. However, according to the definition of the vibration envelopes given by Chaplin et al. (2005), they are merely the maximum and minimum responses of the riser over the entire simulation period. In other words, the envelopes are not detailed representations of the quality of the responses as the maximum or minimum responses can occur along the riser at different times during the simulation period. Simply extracting the maximum and minimum amplitudes from the simulation would not produce the mode shapes of interest.

Aside from the post-processing aspects, the experimental VIV coefficients adopted in this model might also be a small limiting factor. Those coefficients were collected from one-dimensional forced oscillation experiments in which the test specimen was only subjected to oscillation in the crossflow direction. VIV is known to occur in both the crossflow and inline directions; the accuracy of the current model can be improved with the addition of inline VIV coefficients. Further research may focus on conducting forced oscillation experiments with two degrees of freedom systems from which both crossflow and inline VIV coefficients can be obtained. These coefficients can enhance the current model in the prediction of inline responses as well as crossflow motion.

Chapter 6

Conclusions and Recommendations

A time-domain method was enhanced in this work to simulate riser VIV. This method uses the finite element procedure to discretize the riser with rod elements and adopts a novel VIV forcing algorithm to solve the problem in the time-domain. In the VIV forcing algorithm, hydrodynamic coefficients collected from forced vibration experiments on a rigid pipe were used. A VIV forcing algorithm is adopted in which the state variables of each element in the present cycle is used to interpolate the force coefficients that is to be used for the next vibration cycle. Each cycle is determined by zero-crossing analysis of the crossflow velocity.

This forcing algorithm was implemented in a finite element program, MAPS-Mooring, to perform VIV analyses for deepwater risers. The computation is regarded as a two-step process. The static analysis computes the equilibrium profile of the riser given the boundary conditions, material properties, and static loads. The dynamic analysis solves the equations of motion at each time step.

Validation studies were first conducted on the finite element algorithm by its application to a number of static and dynamic mooring problems. With confidence in the finite element algorithm, validation was extended to the VIV of a rigid pipe with spring boundary conditions as well as a laboratory scale top-tensioned riser. The rigid pipe VIV results were shown to match the experimental results well - and thus

validated the VIV forcing algorithm. The TTR results were in general agreement with the published experimental and numerical results on the same riser.

In the present model, the correlation between neighboring elements is implicitly included through structural response; therefore, no assumption was made on the correlation length. Further investigation should be made to confirm the validity of this statement.

The model should be extended to simulate the behaviour of risers with add-on devices such as strakes and fairings. This would require a different database of hydrodynamic coefficients. The current work focused on riser VIV without add-on devices.

Further validation study should be conducted when more benchmark data becomes available. Research can also be extended to physical VIV experiments. This is quite costly, but data from physical experiments would be very useful for calibrating and validating numerical models.

The present hydrodynamic database was collected on a solid riser segment using forced VIV experiments. The database includes over 200 experimental runs, corresponding to each set of state variable. These experiments are expensive and tedious. An alternative to this is to carry out such experiments using CFD. Using the same setup and forcing as in the physical experiments, these hydrodynamic coefficients can be obtained using CFD programs such as ANSYS CFX and StarCCM+. The current database on solid pipes can be used to calibrate the CFD model. Once calibrated, the model can be extended to riser segments with various properties. These hydrodynamic coefficients can then be used as input in the current program to simulate risers with various properties.

An investigation should be conducted using beam elements, which have both translational and rotational degrees of freedom, instead of the rod elements. The rod element, as adopted in this research, does not take rotational degrees of freedom into account, and therefore some details of rotation might not be captured in the

current model.

Finally, the design of risers is not a stand alone process. It must also take into account the responses of the floater and the mooring system. It would be desirable to incorporate this program into a time-domain floater motion and time-domain mooring program. This would yield a coupled time-domain floater-mooring-riser program. Such a program is useful throughout the riser design process, which gives designers an insight of how the entire system behaves under certain environmental conditions.

References

- Allen, D.W., 1998, "Vortex-Induced Vibration of Deepwater Risers", *Proceedings of the Offshore Technology Conference*, Houston, USA.
- Allen, D.W. and Henning, D.L., 1997, "Vortex-Induced Vibration of a Flexible Smooth Cylinder at Supercritical Reynolds Numbers", *Proceedings of the Seventh International Offshore and Polar Engineering Conference*, Honolulu, USA.
- Atluri, S., Rao, V.K. and Dalton, C., 2009, "A Numerical Investigation of the Near-wake Structure in the Variable Frequency Forced Oscillation of a Circular Cylinder", *Journal of Fluids and Structures*, Vol. 25, pp.229-244.
- Bai, Y. and Bai, Q., 2005, "Subsea Pipelines and Risers", *Ocean Engineering Series*, Elsevier.
- Barrero-Gil, A. and Fernandez-Arroyo, P., 2010, "Fluid Excitation of an Oscillating Circular Cylinder in Cross-flow", *European Journal of Mechanics B/Fluids*.
- Bearman, P.W., Graham, J.M.R. and Obasaju, E.D., 1984, "A model equation for the transverse forces on cylinders in oscillatory flows", *Applied Ocean Research*, Vol. 6.
- Beer, G., Smith, I.M. and Duenser, C., 2008, "The Boundary Element Method with Programming", Springer, New York.
- Bishop, R.E.D., Hassan, A.Y., 1964, "The lift and drag forces on a circular cylinder oscillating in a flowing fluid. *Proc. the Royal Society of London Series A* Vol. 277.

Blevins, R.D., 1990, 'Flow-Induced Vibration', *Van Nostrand Reinhold*, New York, USA.

Boster, P., Burke, R., Kavanagh, K., O'Sullivan, E., Picksley, J., Song, R., Stanton, P. and Wald, G., 2004, "Fundamentals of Deepwater Riser Engineering", *Lecture Notes*, Houston, Texas, USA.

Brika, D. and Laneville, A., 1993, "Vortex-Induced Vibrations of a Long Flexible Circular Cylinder", *Journal of Fluid Mechanics*.

Carberry, J., Govardhan, R., Sheridan, J., Rockwell, D. and Williamson, C.H.K., 2004, "Wake States and Response Branches of Forced and Freely Oscillating Cylinders", *European Journal of Mechanics B/Fluids*, Vol. 23.

Carmo, B.S., Sherwin, S.J., Bearman, P.W. and Willden, R.H.J., 2011, "Flow-induced Vibration of a Circular Cylinder Subjected to Wake Interference at Low Reynolds Number", *Journal of Fluids and Structures*, Vol. 27.

Chaplin, J.R., Bearman, P.W., Huera Huarte, F.J. and Pattennden, R.J., 2005a, "Laboratory Measurements of Vortex-induced Vibrations of a Vertical Tension Riser in a Stepped Current", *Journal of Fluids and Structures*, Vol. 21.

Chaplin, J.R., Bearman, P.W., Cheng, Y., Fontaine, E., Graham, J.M.R., Herfjord, K., Hurta Huarte, F.J., Isherwood, M., Lambrakos, K., Larsen, C.M., Meneghini, J.R., Moe, G., Pattenden, R.J., Triantafyllou, M.S. and Willden, R.H.J., 2005b, "Blind Predictions of Laboratory Measurements of Vortex-induced Vibrations of a Tension Riser", *Journal of Fluids and Structures*, Vol. 21.

Dahl, H.M., 2008, "Vortex-Induced Vibration of a Circular Cylinder with Combined In-line and Cross-flow motion", *PhD Thesis*, Massachusetts Institute of Technology, Massachusetts, USA.

Faltisen, O.M., 1990, "Sea Loads on Ships and Offshore Structures", *Cambridge University Press*, Cambridge, UK.

Faure, T., 1989, "Experimental and Numerical Investigation of Mooring Line Dynamics", *NRC Technical Report*, Ottawa, Canada.

Ferziger, J.H. and Perić, M., 2002, *Computational Methods for Fluid Dynamics*, Springer-Verlag, Germany.

Flemming, F. and Williamson, C.H.K., 2005, "Vortex-Induced Vibrations of a Pivoted Cylinder", *Journal of Fluid Mechanics*, Cambridge University Press.

Garrett, D.L., 1982, "Dynamic Analysis of Slender Rods", *Proc. of the 1st International Offshore Mechanics and Arctic Engineering Symposium*, Dallas, USA.

Ghimire, A., 2008, "A Parametric Study of Vortex-Induced Vibration of a Long Flexible Marine Riser", *M. Eng Thesis*, Memorial University of Newfoundland, St. John's, Canada.

Gopalkrishnan, R., 1993, "Vortex-Induced Forces on Oscillating Bluff Cylinders", *PhD Thesis*, Woods Hole Oceanographic Institution and Massachusetts Institute of Technology, Massachusetts, USA.

Grant, R., Litton, R., Finn, L., Maher, J. and Lambrakos, K., 2000, "Highly Compliant Rigid Risers: Field Test Benchmarking a Time Domain VIV Algorithm", *Proceedings of the Offshore Technology Conference*, Houston, USA.

Halse, K.H., 2000, "Norwegian Deepwater Program: Improved Predictions of Vortex-Induced Vibrations", *Proceedings of the Offshore Technology Conference*, Houston, USA.

He, C., Duan, Z. and Ou, J., 2010, "Numerical Simulation of Vortex-induced Vibrations on a Flexible Riser in Uniform Currents", *Proc. of 29th Conference Offshore Mechanics and Arctic Engineering*, Shanghai, China.

Huang, K., Chen, H.C., and Chen, C.R., 2007, "Deepwater Riser VIV Assessment by Using a Time Domain Simulation Approach", *Proceedings of the Offshore Technology Conference*, Houston, USA.

Huang, K., Chen, H.C. and Chen, C.R., 2010, "Vertical Riser VIV Simulation in Uniform Current", *Journal of Offshore Mechanics and Arctic Engineering*, Vol. 132.

Huse, E., 1998, "Large Scale Model Testing of Deep Sea Risers", *Proceedings of the Offshore Technology Conference*, Houston, USA.

Iwan, W.D. and Blevins, R.D., 1974, "A Model for Vortex Induced Oscillation of Structures" *Journal of Applied Mechanics*, Vol. 41

Jauvtis, N. and Williamson, C.H.K., 2003, "Vortex-Induced Vibration of a Cylinder with Two Degrees of Freedom", *Journal of Fluids and Structures*.

Jauvtis, N. and Williamson, C.H.K., 2004, "The Effect of Two Degrees of Freedom on Vortex-Induced Vibration at Low Mass and Damping", *Journal of Fluid Mechanics*, Cambridge University Press.

Jong, J.Y. and Vandiver, J.K., 1983, "Response Analysis of the Flow-Induced Vibration of Flexible Cylinders Tested at Castine, Maine in July and August of 1981", Massachusetts Institute of Technology, Cambridge, Massachusetts.

Khalak, A. and Williamson, C.H.K., 1999, "Motions, Forces and Mode Transitions in Vortex-Induced Vibrations at Low Mass-Damping", *Journal of Fluids and Structures*.

Kim, W.J., 2001, "Coupled Cross-Flow and In-line Vortex-Induced Vibration of Elastic Cable Systems", *PhD Thesis*, University of Michigan,

King, R., 1977, "A Review of Vortex Shedding Research and Its Application", *Ocean Engineering*, Vol. 4.

Kitney, N. and Brown, D.T., 2001, "Experimental Investigation of Mooring Line Loading using Large and Small-Scale Models", *Journal of OMAE*, Vol. 123.

Larsen, C.M. and Halse, K.H., 1997, "Comparisons of Models for Vortex Induced Vibrations of Slender Marine Structures", *Marine Structures*, Vol. 10.

Leonard, A. and Roshko, A., 2001, "Aspects of Flow-Induced Vibration", *Journal of Fluids and Structures*, Vol. 15.

Li, X.Q., 2005, "Identification of Linear and Non-linear Multi-Modal VIV Responses

for Flexible Deepwater Risers", *PhD Thesis*, Memorial University of Newfoundland, St. John's, Canada.

Lie, H., Ciappi, E., Huang, S., Hong, S. and Zhi, Z., 2011, "The Specialist Committee on Vortex Induced Vibrations", *Proceedings of 26th ITTC Conference*, Rio de Janeiro, Brazil.

Ma, P. and Qiu, W., 2010, "Validation studies for MAPS-Mooring Version 1.0", *Technical Report AMHL-10-01*, Advanced Marine Hydrodynamics Laboratory, Faculty of Engineering and Applied Science, Memorial University of Newfoundland, St. John's, Canada.

Marcollo, H., Chaurasia, H., and Vandiver, J.K., 2007, "Phenomena Observed in VIV Bare Riser Field Tests", *Proceedings of the 26th International Conference on Offshore Mechanics and Arctic Engineering*, San Diego, California, USA.

Masuda, K., Ikoma, T., Kondo, N. and Maeda, H., 2006, "Forced Oscillation Experiments for VIV of Circular Cylinders and Behaviors of VIV and Lock-in Phenomenon", *Proceedings of the 25th International Conference on Offshore Mechanics and Arctic Engineering*, Hamburg, Germany.

Moe, G. and Wu, Z.J., 1989, "Lift Force on a Vibrating Cylinder in a Current", *Proceedings of the Eighth International Conference on Offshore Mechanics and Arctic Engineering*

Murrin, D., 2007, "A Three-dimensional Simulation of Vortex Induced Vibrations (VIV) on Marine Risers at High Reynolds Number using Computational Fluid Dynamics", *PhD Thesis*, Memorial University of Newfoundland, St. John's, Canada.

Murrin, D., Molloy, S., Qiu, W., Bose, N. and Ordonez, M., 2008, "Large-Scale Experiments of a Marine Riser", *Proceedings of Oceans 2008 MTS/IEEE Conference*, Quebec City, Canada.

Murrin, D., Ordonez, M., Stone, G., Bose, N. and Qiu, W., 2007, "High Mode Vortex Induced Vibration (VIV) Experiments on a Large-Scale Riser", *Proceedings of Oceans 2007 MTS/IEEE Conference*, Vancouver, Canada.

Nordgren, R.P., 1974, "On Computation of the Motion of Elastic Rods," *Journal of Applied Mechanics*, Transaction of ASME, Vol. 41.

Ormberg, H., Fylling, I.J. and Morch, M., 1983, "Dynamic Response in Anchor Lines: Numerical Simulation Compared with Field Measurements, Paper No. 4497, Offshore Technology Conference, Houston, USA.

Press, W., Teukolsky, S.A., Vetterling, W.T. and Flannery, B.P., "Numerical Recipes in Fortran 90", Cambridge University Press, USA.

Randall, R.E., 1997, "Elements of Ocean Engineering", *Society of Naval Architects and Marine Engineers*, New York, USA.

Sanchis, A., Salevik, G. and Grue, J., 2008, "Two-degree-of-freedom Vortex-Induced Vibrations of a Spring-Mounted Rigid Cylinder with Low Mass Ratio", *Journal of Fluids and Structures*, Vol. 24.

Sarpkaya, T., 1978, "Fluid Forces on Oscillating Cylinders", *ASCE Journal of Waterway, Port, Coastal, and Ocean Division*, Vol. 104.

Schulz, K.W., 1999, "Numerical Prediction of the Hydrodynamic Loads and Motions of Offshore Structures", *PhD Thesis*, University of Texas, Austin, USA.

Sidarta, D.E., Finn, L.D. and Maher, J., 2010, "Time Domain FEA for Riser VIV Analysis", *Proc. of the 2010 OMAE Conference*, Shanghai, China.

Spencer, D., 2009, Oceanic Consulting Corporation, Private Communication.

Spencer, D., Hui, Y. and Qiu, W., 2007, "Development and Verification of a Time-Domain VIV Simulation Tool", *Proc. 3rd International Workshop on Applied Offshore Hydrodynamics*, Rio de Janeiro, Brazil.

Staubli, T., 1983, "Calculation of the Vibration of an Elastically Mounted Cylinder Using Experimental Data From Forced Oscillation", *Journal of Fluids Engineering*, Vol. 105.

Stone, G., 2008, "The Design, Assembly and Testing of a Large Scale Model Riser for Vortex Induced Vibrations", *M.Eng Thesis*, Memorial University of Newfoundland, St. John's, Canada.

Triantafyllou, G., Triantafyllou, M. and Chryssostomidis, C., 1986, "On the formation of Vortex Street Behind Stationary Cylinders", *Journal of Fluid Mechanics*, Vol 170.

Vandiver, J.K. 1983, "Drag Coefficients of Long Flexible Cylinders", *Proceedings of the Offshore Technology Conference*, Houston, USA.

Vandiver, J.K. 1993, "Dimensionless Parameters Important to the Prediction of Vortex-Induced Vibration of Long, Flexible Cylinders in Ocean Currents", *Journal of Fluids and Structures*, Vol. 7.

Vandiver, J. K. and Li, L., 2005, "Shear7 V4.4 Program Theoretical Manual", Department of Ocean Engineering, Massachusetts Institute of Technology.

Vandiver, J.K. and Marcollo, H., 2003, "High Mode Number VIV Experiments", *IUTAM Symposium On Integrated Modeling of Fully Coupled Fluid-Structure Interactions Using Analysis, Computations, and Experiments*, Kluwer Academic Publishers, Dordrecht.

Vandiver, J.K. and Jong, J.Y., 1987, "The Relationship between In-line and Cross-flow Vortex-Induced Vibration of Cylinders", *Journal of Fluids and Structures*, Vol. 1.

Venugopal, M., 1996, "Damping and Response Prediction of a Flexible Cylinder in a Current", *PhD Thesis*, Massachusetts Institute of Technology, Massachusetts, USA.

Vikestad, K., Larsen, C.M. and Vandiver, J.M., 1997, "Experimental Study of Excited Circular Cylinders in Current", *Proceedings of the 16th International Conference on Offshore Mechanics and Arctic Engineering*

Vikestad, K., Larsen, C.M. and Vandiver, J.M., 2000, "Norwegian Deepwater Program: Damping of Vortex-Induced Vibrations", *Proceedings of the Offshore Technology Conference*, Houston, USA.

Vikestad, K. and Halse, K.H., 2000, "VIV Lift Coefficients Found from Response

Build-up of an Elastically Mounted Dense Cylinder”, *Proceedings of the 10th International Offshore and Polar Engineering Conference*, Seattle, USA.

Vikestad, K. and Halse, K.H., 2000, “Effect of Variable Current on Vortex-Induced Vibrations”, *Proceedings of the 10th International Offshore and Polar Engineering Conference*, Seattle, USA.

Williamson, C.H.K. and Govardhan, R., 2008, “A Brief Review of Recent Results in Vortex-Induced Vibrations”, *Journal of Wind Engineering and Industrial Aerodynamics*, Vol. 96.

Xue, J., 2006, “Particle Image Velocimetry Investigation of the Wake Fields of a Long Flexible Riser”, *M.Eng Thesis*, Memorial University of Newfoundland, St. John's, Canada.

Xue, J., He, M. and Bose, N., 2009, “Vortex Modes and Vortex-Induced Vibration of a Long, Flexible Riser”, *Ocean Engineering*, Vol. 36.

Yin, H. and Qiu, W., 2007, “Dynamic Analysis of Mooring Lines in the Time Domain”, *Proc. of the 8th Canadian Marine Hydromechanics and Structures Conference*, St. John's, Canada.

Zhu, L., 2006, “Model Riser Test for Vortex Induced Vibration in a Sheared Current”, *M.Eng Thesis*, Memorial University of Newfoundland, St. John's, Canada.

Appendix A

Mathematical Formulation

This chapter provides a description of the mathematical formulation employed to address the riser VIV phenomenon. The equations of motion (EoM) are derived based on the theory of rods. By extending the theory to consider large deflections, bending stiffness and tension variation across the riser, the EoM may be employed to capture the highly nonlinear VIV problem.

A.1 Coordinate System

A 3D Cartesian coordinate system with the xoy plane resting on the undisturbed free surface and z -axis positive upwards is adopted in this formulation. The position of a segment of the riser, represented by the vector $\mathbf{r}(s, t)$, are both time t and arclength s dependent. Defining a unit tangent vector along the riser as $\mathbf{r}' = \frac{d\mathbf{r}}{ds}$, the principal normal vector as $\mathbf{r}'' = \frac{d^2\mathbf{r}}{ds^2}$, and denoting the bi-normal vector is along the direction of $\mathbf{r}' \times \mathbf{r}''$.

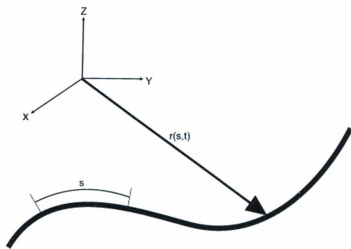


Figure A-1: Coordinate System

A.2 Equations of Motion

Assuming a segment of the riser behaves as a slender rod and considering momentum conservation, the equations of motion is derived as

$$F' + q = \rho \ddot{r} \quad (\text{A.1})$$

$$M' + r' \times F + m = 0 \quad (\text{A.2})$$

where \mathbf{F} is the resultant force, \mathbf{M} is the resultant moment at a position of the rod acting along the centerline, \mathbf{q} is the applied force per unit length, \mathbf{m} is the applied moment per unit length, ρ is the mass per unit length, the prime denotes the partial derivatives with respect arclength s while the superposed dots denote the time derivatives.

For an elastic rod with equal principal stiffness, the bending moment is proportional to curvature and acts in the direction of the binormal vector. The

resultant moment can then be represented as

$$M = r' \times EIr'' + Hr' \quad (\text{A.3})$$

where E is the elastic modulus of the material that makes up the rod, I is the moment of inertia of the cross section of the rod, and H is the torque. EI is also known as the bending stiffness of the elastic rod. Substitute Equation A.3 into Equation A.2 gives

$$(r' \times EIr'' + Hr')' + r' \times F + m = 0 \quad (\text{A.4})$$

$$r' \times (EIr''') + r'' \times r'' + H'r' + Hr'' + r' \times F + m = 0 \quad (\text{A.5})$$

Invoking $r'' \times EIr'' = 0$ and grouping the terms yield

$$r' \times [(EIr''')' + F] + H'r' + Hr'' + m = 0 \quad (\text{A.6})$$

The scalar product of Equation A.6 and r' gives

$$r' \cdot r' \times [(EIr''')' + F] + r' \cdot H'r' + r \cdot Hr'' + r' \cdot m = 0 \quad (\text{A.7})$$

This can be rewritten as Equation A.8 by considering $r' \cdot r' = 1$, $r' \cdot r' \times [(EIr''')' + F] = 0$, and $r \cdot Hr'' = 0$.

$$H' + m \cdot r' = 0 \quad (\text{A.8})$$

Consider risers to have circular cross sections, one may assume there will not be any distributed torsional moment ($m \cdot r'$) from hydrodynamic loads. It can then be devised that the torque H is independent of arclength s based on Equation A.8. The torque is assumed to be negligible. Thus both H and m are zero. This leads to the

simplification of Equation A.6 as

$$r' \times [(EIr''')' + F] = 0 \quad (\text{A.9})$$

The vector $(EIr''')' + F$ is directed along the centerline of the rod. This vector is then equivalent to the scalar product of r' and some scalar function $\lambda(s, t)$,

$$(EIr''')' + F = \lambda r' \quad (\text{A.10})$$

Taking the dot product of Equation A.10 and r' gives

$$\lambda = F \cdot r' + (EIr''')' \cdot r' \quad (\text{A.11})$$

EI is assumed to be constant for the rod segment, and $r' \cdot r''' = (r' \cdot r'')' - r'' \cdot r'' = 0 - \kappa^2$, then

$$\lambda = T - EI\kappa^2 \quad (\text{A.12})$$

where T is the tension in the rod and κ is the curvature. Substituting Equation A.10 into Equation A.1 gives the equation of motion governing the rod

$$-(EIr''')'' + (\lambda r')' + q = \rho \ddot{r} \quad (\text{A.13})$$

where \mathbf{r} must comply with the inextensible condition defined as

$$r' \cdot r' = 1 \quad (\text{A.14})$$

Consider the rod is stretchable and the stretch in the axial direction is linear and small (i.e. ϵ), then Equation A.14 can be approximated by

$$r' \cdot r' = (1 + \epsilon)^2 \approx 1 + 2\epsilon = 1 + 2 \frac{T}{EA} \quad (\text{A.15})$$

$$\frac{1}{2}(r' \cdot r' - 1) = \frac{T}{EA} \approx \frac{\lambda}{EA} \quad (\text{A.16})$$

This approximation is valid given that the strain ϵ is small, i.e. the axial stiffness is relatively large compared to the tension in the rod. The Lagrangian multiplier, λ , is a scalar function that arose as a result of the inextensibility assumption. Equations A.13 and A.16 along with initial conditions and boundary conditions are sufficient to compute the dependent variables $r(s, t)$ and $\lambda(s, t)$. The applied load, q , consists of three main sources in offshore applications: the self weight of the cylindrical structure, the hydrostatic load, and the hydrodynamic loads.

$$q = w + F^s + F^d \quad (\text{A.17})$$

where w is the weight per unit length, F^s is the hydrostatic force per unit length and F^d is the hydrodynamic force per unit length. The hydrostatic force is written as

$$F^s = B + (P_s r')' \quad (\text{A.18})$$

where B is the buoyancy force per unit length when the rod is submerged below the free surface. The term $(P_s r')'$ arose due to the pressure gradient between the two ends of the rod, and P_s is the hydrostatic pressure at position r on the rod. The two ends of the rod are not exposed to water, so the pressure force must be subtracted from the total buoyancy force in the computation process. The hydrodynamic force on the rod can be computed using Morison's equation, based on slender body assumption.

$$F^d = -C_A \ddot{r}^n + C_M \dot{V}^n + C_D |V_{rel}^n| V_{rel}^n \quad (\text{A.19})$$

where C_A is the added mass per unit length, C_M is the inertial force per unit length per unit normal acceleration, and C_D is the drag force per unit length per unit normal

velocity. The terms V_{ret}^n and \dot{V}^n are the normal fluid velocity and acceleration, while \dot{r}^n and \ddot{r}^n represent the components of the velocity and acceleration of the rod normal to its centerline.

$$V_{ret}^n = (V - \dot{r}) - [(V - \dot{r}) \cdot r'] \cdot r' \quad (\text{A.20})$$

$$\dot{V}^n = \dot{V} - (\dot{V} \cdot r') \cdot r' \quad (\text{A.21})$$

$$\dot{r}^n = \dot{r} - (\dot{r} \cdot r') \cdot r' \quad (\text{A.22})$$

$$\ddot{r}^n = \ddot{r} - (\ddot{r} \cdot r') \cdot r' \quad (\text{A.23})$$

Substituting Equations A.17, A.18 and A.19 into Equation A.13 gives:

$$\rho \ddot{r} + C_A \ddot{r}^n + (EI r''')^n - (\lambda r')' - (P_s A r')' = w + B + \tilde{F}^d \quad (\text{A.24})$$

where $\tilde{F}^d = C_M \dot{V}^n + C_D |V_{ret}^n| V_{ret}^n$

Introducing

$$\tilde{w} = w + B \quad (\text{A.25})$$

$$\tilde{\lambda} = \lambda + P_s A \quad (\text{A.26})$$

Substituting Equation A.12 into A.26,

$$\tilde{\lambda} = (T + P_s A) - EI \kappa^2 = \tilde{T} - EI \kappa^2 \quad (\text{A.27})$$

Equation A.24 can be rewritten as

$$\rho \ddot{r} + C_A \ddot{r}^n + (EI r'')'' - (\tilde{\lambda} r')' = \tilde{w} + \tilde{F}^d \quad (\text{A.28})$$

\tilde{T} stands for the effective tension in the rod, and \tilde{w} is the effective weight. Consistency must be followed throughout the computation. This means that if the effective weight is used, the computed tension should be the effective tension, which must be converted to obtain the actual tension in the rod. Equations A.28 and A.14 or A.16 form the governing equations for the static and dynamic analysis of risers.

Appendix B

Numerical Methods

B.1 Finite Element Discretization

Equations A.28 and A.16 were solved using the finite element method in the work of Yin and Qiu (2007). The discretization process is summarized here for completeness.

Using Einstein notation, the governing equations can be written as:

$$-\rho \ddot{r}_i - C_A \ddot{r}_i'' - (E I r_i'')'' + (\tilde{\lambda} r_i')' + \tilde{w}_i + \tilde{F}_i^d = 0 \quad (\text{B.1})$$

$$\frac{1}{2}(r_n' r_n' - 1) - \frac{\lambda}{EA} = \frac{1}{2}(r_n' r_n' - 1) - \frac{\tilde{\lambda} - P_s A}{EA} = 0 \quad (\text{B.2})$$

In order to use the finite element procedure, the variables $r_i(s, t)$ and $\tilde{\lambda}(s, t)$ along the element length L can be approximated by

$$r_i(s, t) = A_k(s) U_{ik}(t) \quad i = 1, 2, 3 \quad k = 1, 2, 3, 4 \quad (\text{B.3})$$

$$\tilde{\lambda}(s, t) = P_m(s) \tilde{\lambda}_m(t) \quad m = 1, 2, 3 \quad (\text{B.4})$$

$0 \leq s \leq L$ A_k and P_m are interpolation functions. For the rod element, A_k and P_m

are described by:

$$A_1 = 1 - 3\zeta^2 + 2\zeta^3 \quad (\text{B.5})$$

$$A_2 = \zeta - 2\zeta^2 + \zeta^3 \quad (\text{B.6})$$

$$A_3 = 3\zeta^2 - 2\zeta^3 \quad (\text{B.7})$$

$$A_4 = -\zeta^2 + \zeta^3 \quad (\text{B.8})$$

$$P_1 = 1 - 3\zeta + 2\zeta^2 \quad (\text{B.9})$$

$$P_2 = 4\zeta(1 - \zeta) \quad (\text{B.10})$$

$$P_3 = \zeta(2\zeta - 1) \quad (\text{B.11})$$

where $\zeta = s/L$, U_{ik} and $\tilde{\lambda}_m$ are the coefficients to be solved. On each element with length L ,

$$U_{i1} = r_i(0, t) \quad (\text{B.12})$$

$$U_{i2} = Lr'_i(0, t) \quad (\text{B.13})$$

$$U_{i3} = r_i(L, t) \quad (\text{B.14})$$

$$U_{i4} = Lr'_i(L, t) \quad (\text{B.15})$$

$$\tilde{\lambda}_1 = \tilde{\lambda}(0, t) \quad (\text{B.16})$$

$$\tilde{\lambda}_2 = \tilde{\lambda}(L/2, t) \quad (\text{B.17})$$

$$\tilde{\lambda}_3 = \tilde{\lambda}(L, t) \quad (\text{B.18})$$

The degrees of freedom for a two element analysis is shown in Figure B-1.



Figure B-1: Degrees of freedom for two rod elements

Applying the Galerkin method to the governing equations, the equations of motion become:

$$\int_0^L [A_1(\rho \ddot{w}_i + C_A \ddot{r}_i^n) + EI A_i'' r_i'' + A_i' \tilde{\lambda} r_i' - A_i(\tilde{w}_i + \tilde{F}_i^d)] ds = EI r_i'' A_i|_0^L + [\tilde{\lambda} r_i' - (EI r_i'')] A_i|_0^L \quad (\text{B.19})$$

$$\int_0^L P_m \left[\frac{1}{2} (r_n' r_n' - 1) - \frac{\tilde{\lambda} - P_s A}{EA} \right] ds = 0 \quad (\text{B.20})$$

Substituting the above interpolation functions into Equations B.19 and B.20, the following discretized form of the equations of motion are obtained:

$$(M_{ijkl} + M_{ijkl}^n) \ddot{U}_{jk} + (K_{ijkl}^1 + \tilde{\lambda}_n K_{ijkl}^2) U_{jk} - F_{ij} = 0 \quad (\text{B.21})$$

where

$$M_{ijtk} = \int_0^L \rho A_t A_k \delta_{ij} ds \quad (\text{B.22})$$

$$M_{ijtk}^0 = C_A \left[\int_0^L A_t A_k \delta_{ij} ds - \left(\int_0^L A_t A_k A'_s A'_s ds \right) U_{it} U_{js} \right] \quad (\text{B.23})$$

$$K_{ijtk}^1 = \int_0^L E I A'_i A'_k \delta_{ij} ds \quad (\text{B.24})$$

$$K_{ijtk}^2 = \int_0^L P_n A'_i A'_k \delta_{ij} ds \quad (\text{B.25})$$

$$F_{it} = \int_0^L (\tilde{w}_i + \tilde{F}_i^d) A_t ds \quad (\text{B.26})$$

δ is the Kronecker delta function.

$$G_m = A_{mit} U_{kt} U_{ki} - B_m - C_{mt} \tilde{\lambda}_t + C_{mt} A P_{St} = 0 \quad (\text{B.27})$$

$$A_{mit} = \frac{1}{2} \int_0^L P_m A'_i A'_i ds \quad (\text{B.28})$$

$$B_m = \frac{1}{2} \int_0^L P_m ds \quad (\text{B.29})$$

$$C_{mt} = \frac{1}{EA} \int_0^L P_m P_t ds \quad (\text{B.30})$$

where $m = 1, 2, 3$ and $i, l = 1, 2, 3, 4$.

$$P_s = P_m P_{Sm} \quad (\text{B.31})$$

$$P_{S1} = P_s(0, t) \quad (\text{B.32})$$

$$P_{S2} = P_s(L/2, t) \quad (\text{B.33})$$

$$P_{S3} = P_s(L, t) \quad (\text{B.34})$$

the hydrostatic pressure P_s is defined as ρgh or $-\rho gr_3$.

Using the interpolation or approximation functions, the pressure terms can be expressed as

$$P_{S1} = -\rho g U_{31} \quad (\text{B.35})$$

$$P_{S2} = -\rho g (0.5U_{31} + 0.125U_{32} + 0.5U_{33} - 0.125U_{34}) \quad (\text{B.36})$$

$$P_{S3} = -\rho g U_{33} \quad (\text{B.37})$$

From the discretized form of the governing equations, there are 12 second-order ordinary differential equations and 3 algebraic equations to be solved in this formulation.

B.2 Formulation for Static Analysis

The static analysis is done by neglecting the inertial term in the governing equation (Equation B.21). The reduced form of the discretized equation are as follows:

$$R_{il} = (K_{ijk}^1 + \tilde{\lambda}_n K_{nijl}^2) U_{jk} - F_{il} = 0 \quad (\text{B.38})$$

$$G_m = A_{mkl} U_{kl} U_{kl} - B_m - C_{mt} \tilde{\lambda}_t + C_{mt} A P_{St} = 0 \quad (\text{B.39})$$

F_{il} includes all static forces such as gravity, drag due to steady current, and any other applied static forces on the riser.

Newton's method is used to iteratively solve the nonlinear equations. Applying Taylor's series expansion, and neglecting higher order terms, the above equations are approximated using the estimated solution or solution from the previous n^{th} iteration, i.e. $U^{(n)}$ and $\tilde{\lambda}^{(n)}$ can be expressed as:

$$R_{il}^{n+1} = R_{il}^n + \frac{\partial R_{il}}{\partial U_{jk}}(\Delta U_{jk}) + \frac{\partial R_{il}}{\partial \tilde{\lambda}_n}(\Delta \tilde{\lambda}_n) = 0 \quad (\text{B.40})$$

$$G_m^{n+1} = G_m^n + \frac{\partial G_m}{\partial U_{jk}}(\Delta U_{jk}) + \frac{\partial G_m}{\partial \tilde{\lambda}_n}(\Delta \tilde{\lambda}_n) = 0 \quad (\text{B.41})$$

There are 15 linear algebraic equations to be computed for each element at every iteration. In the work of Yin and Qiu(2007), a renumbering technique was used to convert the degrees of freedom of U and $\tilde{\lambda}$ into a one dimensional array. This operation converts the above equations into

$$[K^{(n)}](\Delta y) = F^{(n)} \quad (\text{B.42})$$

and it was subsequently solved using a Gaussian Elimination solver for banded matrices. The flowchart for static analysis is shown in Figure B-2. The static problem is solved by iteration. The solution is achieved once the computed configuration and tension are within a user-specified tolerance.

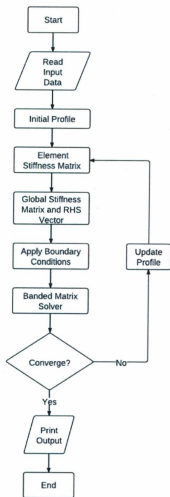


Figure B-2: Flow Chart for Static Analysis

B.3 Formulation for Dynamic Analysis

The dynamic analysis requires the time integration of the governing equations B.21 and B.27. Equation B.21 can be rewritten as,

$$(\hat{M}_{ijk})\ddot{U}_{jk} = -(K_{ijk}^1 + \tilde{\lambda}_n K_{nijk}^2)U_{jk} + F_{it} \quad (\text{B.43})$$

$$= -F_{it}^1 - F_{it}^2 + F_{it}^* = \hat{F}_{it} \quad (\text{B.44})$$

This second order ordinary differential equation can be converted to a system of two first order equations as follows,

$$(\hat{M}_{ijk})\dot{V} = \hat{F}_{it} \quad (\text{B.45})$$

$$\dot{U}_{jk} = V_{jk} \quad (\text{B.46})$$

The time integration of these two equations from time step (n) to (n+1) is done using the second order Adams-Moulton method. The mass term \hat{M}_{ijk} , that includes both the body mass and added mass of the element is done using the Adams-Bashforth explicit scheme. Forces such as F_{it}^1 and F_{it}^2 , being constant for each time interval, are integrated using Adams-Moulton method. The hydrodynamic force F_{it} , computed from Morison's Equation, is integrated using the Adams-Bashforth explicit scheme since it is unknown at time (n+1). The governing equations can then be converted to a system of linear equations (similar to static analysis) as

$$\hat{K}_{ijk}^{t0(n)} \Delta U_{jk} + \hat{K}_{ijk}^{t1(n)} \Delta \tilde{\lambda}_n = \hat{F}_{it}^{(n)} \quad (\text{B.47})$$

and the stretch condition G_m^{n+1} at time step (n+1) can be approximated from G_m^n at time step (n) using Taylor Expansion.

$$\hat{D}_{ijk}^{t0(n)} \Delta U_{jk} + \hat{D}_{ijk}^{t1(n)} \Delta \tilde{\lambda}_n = \hat{G}_m^{(n)} \quad (\text{B.48})$$

where

$$\hat{K}_{ijk}^{t0(n)} = \frac{2}{\Delta t^2} (3\hat{M}_{ijk}^{(n)} - \hat{M}_{ijk}^{(n-1)}) + K_{ijk}^1 + \tilde{\lambda}_n^{(n-\frac{1}{2})} K_{mijk}^2 \quad (\text{B.49})$$

$$\hat{K}_{ijtk}^{t1(n)} = 2K_{nijkl}^2 U_{jk}^n \quad (\text{B.50})$$

$$\hat{D}_{ijtk}^{t0(n)} = 2K_{mijkl}^2 U_{it} \quad (\text{B.51})$$

$$\hat{D}_{ijtk}^{t1(n)} = 2D_{mn}^{t1(n)} \quad (\text{B.52})$$

$$\hat{K}_{it}^{(n)} = \frac{2}{\Delta t^2} (3\hat{M}_{ijk}^{(n)} - \hat{M}_{ijk}^{(n-1)}) V_{jk}^{(n)} + (3F_{it}^{(n)} - F_{it}^{(n-1)}) - 2K_{ijkl}^1 U_{jk}^{(n)} - 2\tilde{\lambda}_n^{(n-\frac{1}{2})} K_{nijkl}^2 U_{jk}^{(n)} \quad (\text{B.53})$$

$$\hat{G}_m^{(n)} = -2G_m^{(n)} \quad (\text{B.54})$$

The detailed integration to obtain the terms in Equations B.49 to B.54 can be found in the work of Yin and Qiu (2007). In his work, a renumbering system was adopted, same as the static analysis, and Equations B.47 and B.48 were expressed as

$$[K^{(n)}] \Delta y = \{F^{(n)}\} \quad (\text{B.55})$$

where

$$\begin{aligned} \{\Delta y\} = & [\Delta U_{11}, \Delta U_{12}, \Delta U_{21}, \Delta U_{22}, \Delta U_{31}, \Delta U_{32}, \Delta \tilde{\lambda}_1, \Delta \tilde{\lambda}_2, \\ & \Delta U_{13}, \Delta U_{14}, \Delta U_{23}, \Delta U_{24}, \Delta U_{33}, \Delta U_{34}, \Delta \tilde{\lambda}_3]^T \end{aligned} \quad (\text{B.56})$$

and

$$\{F^{(n)}\} = [-R_{11}, -R_{12}, -R_{21}, -R_{22}, -R_{31}, -R_{32}, -G_1, -G_2, \\ -R_{13}, -R_{14}, -R_{23}, -R_{24}, -R_{33}, -R_{34}, -G_3]^T \quad (\text{B.57})$$

The logistic of dynamic analysis is given in the flow chart in Figure B-3.

B.4 Boundary Conditions

Boundary conditions can specify basic solution variables (such as displacement and tension) at any nodes. The program can also handle sinusoidal forced motion at the fairlead connection point (i.e. to simulate vessel motion) as well as forces applied at any node.

At both ends of the riser, the program can handle both fixed or free boundary conditions, or a combination of both. If a portion of the riser is lying on the seabed, an elastic layer is used to model the seabed boundary condition. For the elastic layer, the vertical distributed bottom support force (spring) is computed depending on the length of the riser that is in contact with the sea bed. In dynamic analysis, friction forces are also computed as the touchdown points move due to the motion of the riser.

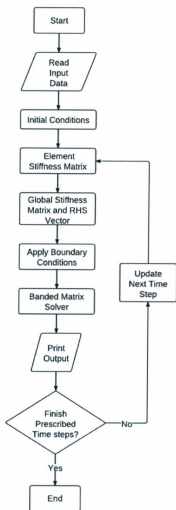


Figure B-3: Flow Chart for Dynamic Analysis

Appendix C

Displacement Time Series Plots

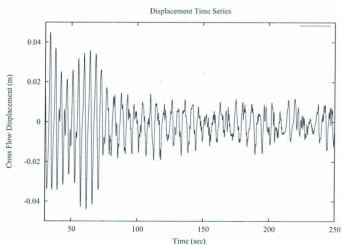


Figure C-1: Case 1 Time Series of Crossflow Vibration at 0.25L

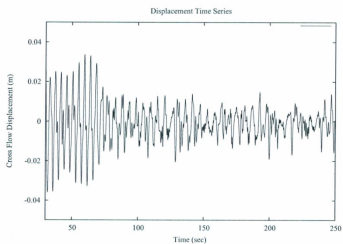


Figure C-2: Case1 Time Series of Crossflow Vibration at 0.75L

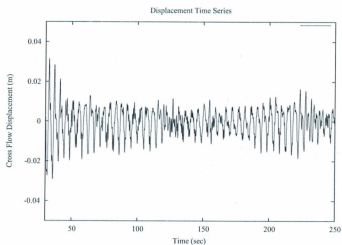


Figure C-3: Case 3 Time Series of Crossflow Vibration at 0.25L

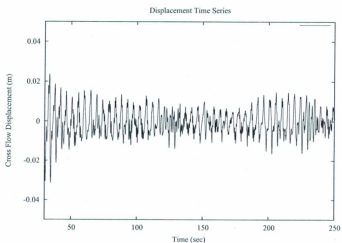


Figure C-4: Case 3 Time Series of Crossflow Vibration at 0.75L

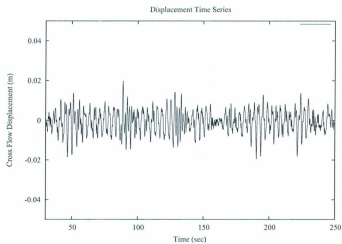


Figure C-5: Case 6 Time Series of Crossflow Vibration at 0.25L

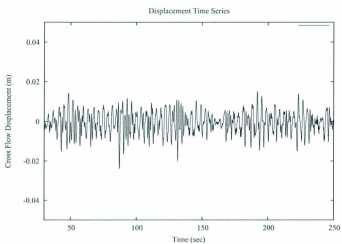


Figure C-6: Case 6 Time Series of Crossflow Vibration at 0.75L

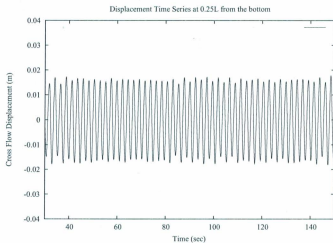


Figure C-7: Case 9 Time Series of Crossflow Vibration at 0.25L

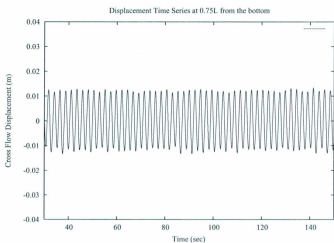


Figure C-8: Case 9 Time Series of Crossflow Vibration at 0.75L



